Plasma regions, charged dust and field-aligned currents near Enceladus

I.A.D. Engelhardt [a,b,*], J.-E. Wahlund [a], D.J. Andrews [a], A.I. Eriksson [a], S. Ye [c], W.S. Kurth [c], D.A. Gurnett [c], M.W. Morooka [d], W.M. Farrell [e], M.K. Dougherty [f]

[a] Swedish Institute of Space Physics, Box 537, SE 751 21 Uppsala, Sweden
[b] Space and Plasma Physics, Department of Physics and Astronomy, Uppsala University, Box 516, SE 751 20 Uppsala, Sweden
[c] Department of Physics and Astronomy, University of Iowa, Iowa City, IA 52242, USA
[d] Laboratory for Atmospheric and Space Physics, University of Colorado Boulder, Boulder, CO 80303, USA
[e] NASA/Goddard Space Flight Center, Greenbelt, MD 20771, USA
[f] The Blackett Laboratory, Imperial College London, SW7 2BZ, UK

A B S T R A C T

We use data from several instruments on board Cassini to determine the characteristics of the plasma and dust regions around Saturn's moon Enceladus. For this we utilize the Langmuir probe and the electric antenna connected to the wideband receiver of the radio and plasma wave science (RPWS) instrument package as well as the magnetometer (MAG). We show that there are several distinct plasma and dust regions around Enceladus. Specifically they are the plume filled with neutral gas, plasma, and charged dust, with a distinct edge boundary region. Here we present observations of a new distinct plasma region, being a dust trail on the downstream side. This is seen both as a difference in ion and electron densities, indicating the presence of charged dust, and directly from the signals created on RPWS antennas by the dust impacts on the spacecraft. Furthermore, we show a very good scaling of these two independent dust density measurement methods over four orders of magnitude in dust density, thereby for the first time cross-validating them. To establish equilibrium with the surrounding plasma the dust becomes negatively charged by attracting free electrons. The dust distribution follows a simple power law and the smallest dust particles in the dust trail region are found to be 10 nm in size as well as in the edge region around the plume. Inside the plume the presence of even smaller particles of about 1 nm is inferred. From the magnetic field measurements we infer strong field-aligned currents at the geometrical edge of Enceladus.

© 2015 Elsevier Ltd. All rights reserved.

1. Introduction

The small icy moon Enceladus is geologically active with long warm fissures at the surface of its south polar region. From there gas and ice grains are continuously being expelled and form a plume (Dougherty et al., 2006; Porco et al., 2006; Spahn et al., 2006; Waite et al., 2006). Many in depth studies have been conducted with various instruments regarding the plume physics based on flyby observations by the Cassini spacecraft (e.g., Spitale and Porco, 2007; Cravens et al., 2009; Krupp et al., 2012). The plume, for instance, has been found to contain partially ionized material including negatively charged nanograins (Jones et al., 2009; Morooka et al., 2011; Shafiq et al., 2011; Hill et al., 2012;

Farrell et al., 2012; Dong et al., 2015), where the densities of electrons, ions and negatively charged dust increase to several orders of magnitude compared to the surrounding magnetosphere of Saturn. Newly ejected material from the plume (both ions and charged dust) becomes picked up and accelerated by the Kronian magnetospheric flow (e.g., Tokar et al., 2006, 2008; Pontius and Hill, 2006; Fleshman et al., 2010; Farrell et al., 2012). Enceladus is therefore the primary source of sub-micron sized dust in the E-ring (e.g., Kurth et al., 2006; Spahn et al., 2006), which consists predominantly of negatively charged water ice (Kempf et al., 2006; Hillier et al., 2007), and plays an important role in the dust plasma interaction there (Wahlund et al., 2005, 2009).

Enceladus and its electrically conductive plume act as an obstacle to Saturn's magnetospheric plasma flow, and causes large scale perturbations around the moon (e.g., Dougherty et al., 2006; Saur et al., 2007). The magnetospheric flow slows down due to mass loading of material from the plume, and results in a magnetic field pile-up region upstream of Enceladus' plume (Dougherty

et al., 2006; Morooka et al., 2011). The neutral-ion collisions generate perpendicular (Pedersen and Hall) currents inside the plume, which are then thought to close along the magnetic field lines (Kriegel et al., 2011; Simon et al., 2014) and cause an auroral footprint in Saturn's ionosphere (Pryor et al., 2011). Clear signatures of accelerated electrons are observed at the edges of the plume, which are associated with auroral hiss emissions (Gurnett et al., 2011; Leisner et al., 2013). However, these are along wedge shaped regions (the so-called Alfvén wings) similar to those observed at Io (Neubauer, 1980). These Alfvén wings are the magnetic wakes caused by a moving plasma flow around a stationary conductive obstacle, in this case the plume.

Extensive modeling of the magnetospheric plasma interaction with Enceladus and its plume has been undertaken using a range of approaches (see e.g. Jia et al., 2010; Kriegel et al., 2009; Simon et al., 2011), Numerical models utilizing both fluid and hybrid approximations have been produced, along with analytical studies (Simon et al., 2011). These models have recently been extended to include various approaches to the inclusion of the observed negatively charged dust component within the interaction region (Kriegel et al., 2011). Notably, the most important result is that the charged dust has a strong influence on the Enceladus plasma interaction and therefore must be included in such models to have their results approach reality (Omidi et al., 2010, 2012). Nevertheless, significant challenges are presented to empirical models, specifically in simulating a negatively charged dust population both accurately and stably (e.g., Kriegel et al., 2014; Omidi et al., 2012).

In this paper we present data from all 20 flybys of Enceladus by the Cassini spacecraft, showing in particular new high temporal resolution electron density measurements from the RPWS Langmuir probe (LP), micron sized dust measurements by the RPWS electric antenna and compare those to magnetic field measurements by MAG. The measurements are presented in Section 2. The data for the regions studied include the Enceladus trail region as well as the edge of the plume, and are presented in Sections 3 and 4. We conclude the paper with a discussion and conclusion in Sections 5 and 6, respectively. Appendices A–C include detailed information on the Langmuir probe calibration, as well as the derivation of electron and ion density from LP sweeps and error estimations.

2. Measurement description

2.1. Langmuir probe data

The Radio and Plasma Wave Science (RPWS) instrument sensors consists of three electric field antennas, a tri-axial magnetic search coil assembly and a Langmuir probe (LP) (Gurnett et al., 2004). The Langmuir probe is a spherical sensor (diameter $d_{LP} = 5$ cm) located at the end of a 1.5 m boom on the Cassini spacecraft.

The Langmuir probe data used in this study is from two operation modes; a sweep mode, sweeping through -32 V to $+32$ V, and a 20 Hz mode with a constant bias potential at $+11.5$ V. By applying a bias voltage to the probe, charged particles are attracted to or repelled from the probe. This results in a current, I, to the probe which can be described by the orbit motion limited (OML) theory (Mott-Smith and Langmuir, 1926; Medicus, 1962) for the case $r_{LP} \ll \lambda_D$, where r_{LP} is the probe radius and λ_D the Debye length. The OML current due to a particle species α is given

by

$$I_\alpha = \begin{cases} I_{\alpha,o}(1-\chi_\alpha), & \text{attractive potentials}: \chi_\alpha < 0 \\ I_{\alpha,o}e^{-\chi_\alpha}, & \text{repulsive potentials}: \chi_\alpha > 0, \end{cases} \quad (1)$$

with subscript $_\alpha$ being either electrons or ions, q_α the charge of the species and U_{bias} the applied voltage to the probe. The equilibrium current, $I_{\alpha,o}$, is approximated by Fahleson et al. (1974)

$$I_{\alpha,o} \approx n_\alpha q_\alpha A_{LP} \sqrt{\frac{q_\alpha T_\alpha}{2\pi m_\alpha} + \frac{v_\alpha^2}{16}} \quad (2)$$

with n_α the density of the sampled particle species, A_{LP} ($= 4\pi r_{LP}^2$) the surface of the Langmuir probe sphere, T_α the particles temperature expressed in [eV], m_α the mass, v_α the bulk speed of the species and

$$\chi_\alpha = q_\alpha \left(\frac{U_{float} + U_{bias}}{T_\alpha + \frac{m_\alpha v_\alpha^2}{2q_\alpha}} \right) \quad (3)$$

with U_{float} the floating potential of the probe and U_{bias} the applied potential. For the Cassini LP, the spacecraft potential, U_{SC}, relates to the floating potential approximately as

$$(U_{SC} - U_{float}) \approx \frac{5}{6}U_{SC} \cdot \exp(-d_{LP}/\lambda_D) \quad (4)$$

(Gustafsson and Wahlund (2010)) based on inter-calibrations with CAPS/ELS.

A 512 point probe bias voltage sweep between ± 32 V is executed usually every 10 min (every 24 s for targeted flybys). Sweeps can be used to give information on population densities, their temperature and/or drift energy, and the spacecraft potential. See Fig. 1 as an example sweep from flyby E6 taken at the plasma disk just outside Enceladus. The derivation of the electron and ion density can be found in Appendix B.

The main contributions to the LP current in this region are given by

$$I = I_e + I_i + I_{ph}^{s/c} + I_{ph}^p + I_{sec}^{s/c} + I_{sec}^p + I_d. \quad (5)$$

This includes plasma electrons, I_e, plasma ions, I_i, and photoelectrons from the spacecraft and the probe, $I_{ph}^{s/c}$ and I_{ph}^p. Secondary electrons from energetic particle impacts, $I_{sec}^{s/c}$ and I_{sec}^p, from both spacecraft and probe as well as charged dust, I_d, contribute.

The interest of this paper lies in the linear part of the sweep current contribution which is due to plasma electrons, I_e. At a positive bias potential, where we take $e = q_e$, the OML current is given by

$$I_e = en_e A_{LP} \sqrt{\frac{eT_e}{2\pi m_e}} \left(1 + \frac{U_{float} + U_{bias}}{T_e} \right) \quad (6)$$

Between sweeps, the Langmuir probe is in its 20 Hz continuous sampling mode, set to a fixed bias potential, U_{bias}, of $+11.5$ V. From Fig. 1 we see that this bias potential, marked by the pink vertical dashed line, is on the attractive (linear) part of the curve (red solid line), so variations of I_e can be taken to reflect variations of n_e in the plasma.

While Eq. (4) takes the effect of the spacecraft on its environment into account, no such considerations are included in the other expressions. To compensate for this, the 20 Hz current is calibrated to electron density by comparison with the RPWS upper hybrid emission data (cf. Appendix A). The associated errors of the presented 20 Hz continuous electron density data are presented in Appendix C.

2.2. RPWS dust data

Dust densities for grains above 1 µm in size are calculated from RPWS antenna measurements sampled by the high resolution wideband receiver (WBR) of the RPWS. Dust impacts on the spacecraft induce voltage pulses that can be translated to dust densities and sizes (Gurnett et al., 1983). The density values are scaled back to 1 µm threshold assuming a power law distribution with an exponent of −4, since particles larger than 1 µm have been measured in the space environment around Enceladus (Ye et al., 2014).

2.3. Magnetometer data

The magnetometer data comes from the Cassini dual technique magnetometer instrument (MAG) package consisting of a fluxgate magnetometer (FGM) and a vector helium magnetometer (VHM). In this paper the data from the fluxgate magnetometer is used. The sample rate varies between 10 and 50 Hz. More details regarding the MAG instrument can be found in Dougherty et al. (2004) and Kellock et al. (1996).

For this study we will use the residual magnetic field in Enceladus interaction coordinates, which is given by

$$\Delta \vec{B} = \vec{B}_{obs} - \vec{B}_{Sat}. \tag{7}$$

Here $\vec{B}_{obs}$ is the measured magnetic field and $\vec{B}_{Sat}$ is Saturn's internal magnetic field as modeled by Burton et al. (2010). Our principal use of magnetic field data is in obtaining rough estimates of the field-aligned current density, to compare with the observed plasma density structures.

The magnetic field measured by the magnetometer is used to estimate the field-aligned current density, through Ampère's law,

$$\vec{j} = \frac{1}{\mu_o}\left(\nabla \times \vec{B}\right), \tag{8}$$

whilst making the assumption that the only contribution to the total current $\vec{j}$ is in the direction along the main magnetic field, $\hat{z}$. We thus follow (e.g. Gurnett et al., 2011) in assuming that outside the plume, currents are likely to be field-aligned. While this is reasonable as significant perpendicular currents require collisions or gradients, this method clearly is approximate, as the full 3D variation of the magnetic field cannot be observed from a single spacecraft. Defining a vector, $\vec{p}$, along the projection of the spacecraft trajectory onto the $\hat{x} - \hat{y}$ plane and a vector, $\vec{q}$, which is both perpendicular to $\vec{p}$ and the background magnetic field B_z, the field aligned component of the current can then be approximately calculated by

$$j_z \approx \frac{1}{\mu_o}\frac{\Delta B_q}{\Delta p} \tag{9}$$

where

$$B_q = B_y\frac{\Delta x}{\Delta p} - B_x\frac{\Delta y}{\Delta p}$$

$$\Delta p = \sqrt{(\Delta x)^2 + (\Delta y)^2}$$

We remind the reader that the underlying assumption will not be valid within the Enceladus plume itself, where the perpendicular current closing the Alfvén wing current system will flow, and therefore the results of this calculation are expected to be essentially meaningless during those flybys that pass through this region. The geometry of the Cassini flybys is such that we anticipate that this technique will in general provide an accurate sense of $\vec{j_z}$, although the absolute magnitude may certainly be inaccurate.

Before calculating $\vec{j_z}$, a low pass filter is applied to the magnetic field in order to remove high frequency waves as well as instrumental artifacts, which would otherwise be significantly amplified in the calculation of the derivatives of $\vec{B}$. The filter used is a Butterworth filter of order $n = 4$, with a normalized cutoff frequency of $Wn = 0.1 \cdot 2/Fs$, where Fs is the sampling frequency, here either 32 Hz or 16 Hz depending on the instrument mode on a given flyby.
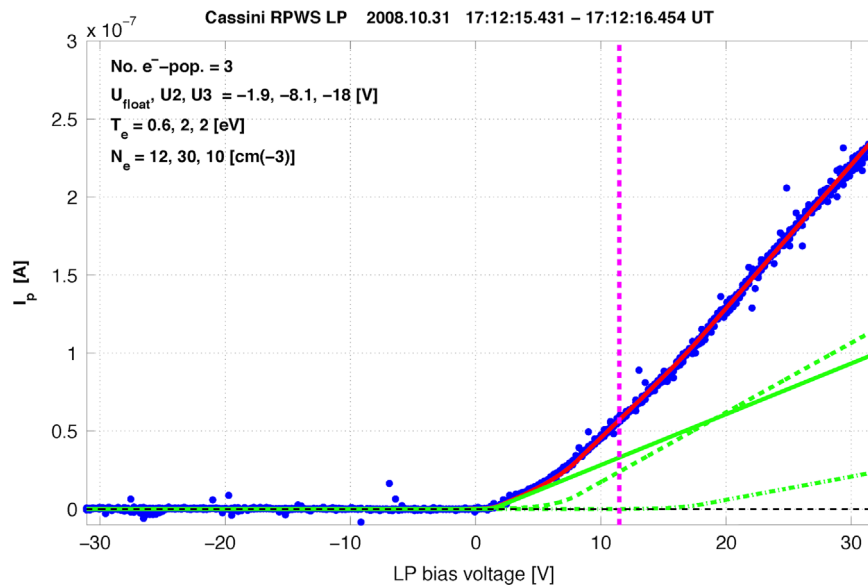

Fig. 1. Example sweep for Flyby E6. The data points (blue) show the sweep data. The total OML fit (red solid line) is a sum of contributions from different electron populations. The first population is due to photoelectrons (green solid line) while also a second and third population (green dashed lines) contribute to the total fit. The parameters for the different populations fits are given in the upper left corner. The bias voltage of +11.5 V (pink dashed line) lies in the linear, attractive part of the curve. (For interpretation of the references to color in this figure caption, the reader is referred to the web version of this paper.)
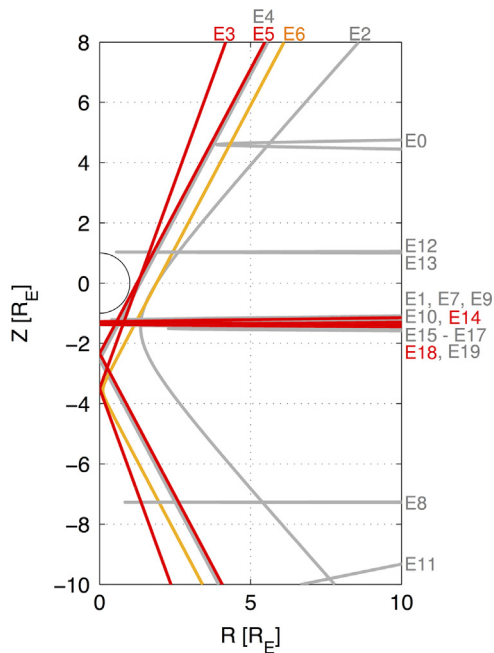
Fig. 2. Overview of all 20 flybys in cylindrical coordinates along the north/south axis of Enceladus. The flybys marked in red are chosen for extended presentation in this study while flyby E6 is used as an example for calibration and error. The gray flybys show the trajectory of all other available flybys. (For interpretation of the references to color in this figure caption, the reader is referred to the web version of this paper.)

3. Detailed observations

3.1. Overview

We have analyzed all 20 targeted Enceladus flybys occurring in the years 2005–2012. Fig. 2 shows the trajectory of all flybys in the Enceladus interaction coordinate system (ENIS coordinates, where $\hat{x}$ is along the ideal magnetospheric corotation direction, $\hat{y}$ is towards Saturn and $\hat{z}$ concludes the right handed system in the north/south direction of Enceladus). The flybys marked in red are chosen for extended presentation in this paper while the flyby E6 (orange) is used in A and C. The coverage of these 20 flybys consists of 12 flybys through the plume of which four flybys (E3, E4, E5, E6) are high inclination flybys that also pass through the Enceladus trail region. Six of those 12 plume passing flybys (E7, E9, E14, E17, E18, E19) are close horizontal flybys in the southern hemisphere (parallel to the equatorial plane and below a closest approach altitude of 100.5 km) and two flybys (E8, E11) pass through the plume at larger distances from Enceladus. Of the remaining eight flybys, there are two close (E12, E13) and one far (E0) horizontal flyby in the northern hemisphere. There exist one close flyby (E2) that is at high inclination upstream of Enceladus and four are horizontal in the southern hemisphere, but not passing through the plume; three flybys (E1, E10, E16) are upstream and the last one (E15) is downstream of Enceladus. There is a scarce coverage upstream as well as in the northern hemisphere close to Enceladus.

We have chosen four flybys that represent regions to be discussed (see Table 1). Two of these flybys, E3 and E5, are high inclination flybys which pass through both the plume and the Enceladus trail region (both analyzed by e.g. Morooka et al., 2011). The two other flybys, E14 and E18, are parallel to Enceladus' equatorial plane that pass through the plume with closest approach altitudes of 99 km and 74 km, respectively. Flyby E14 was in eclipse indicating a main ionization source, like supra-thermal electrons, other than solar EUV.

Table 1
List of flybys presented in more detail in this paper. Details such as the flyby number, the revolution number, the date as well as the day of the year (doy), the closest approach (CA) time and altitude and the average spacecraft speed relative to Enceladus are shown.

Flyby	Rev	Date	DoY	CA Time	CA Alt (km)	$\langle v_{s/c} \rangle$ (km/s)
E3	061	2008–03–12	072	19:06:12	47.674	14.4
E5	088	2008–10–09	283	19:06:40	24.586	17.7
E6	091	2008–10–31	305	17:14:51	169.073	17.7
E14	154	2011–10–01	274	13:52:26	98.906	7.5
E18	164	2012–04–14	105	14:01:38	74.104	7.5

We specifically show a collection of measurements for these selected flybys (E3, E5, E14 and E18) in Figs. 3, 4, 5 and 6, respectively. Each figure has the same format. In these figures panel (a) displays thermal plasma densities; electron density (black and blue) and ion density (red). The electron density in the upstream surrounding magnetosphere is in the range of $\sim$40–110 cm^{-3} during the Enceladus flybys. Panel (b) adds the dust density measurements of dust larger than 1 μm as measured by the RPWS. Note however that the unit here is in m^{-3} compared to panel (a), given in cm^{-3}. Panels (c) and (d) show the residual magnetic field as described in Section 2.3. Away from the interaction region, the value of $\Delta B_z \sim 15$ nT, which is largely due to the field of the Saturnian ring current, centered some distance outside the Enceladus interaction region. Panel (e) shows the estimated field-aligned current (cf. Section 2.3). The last panel (f) shows Cassini's position relative to Enceladus as defined from ENIS and $R = \hat{x}^2 + \hat{y}^2 + \hat{z}^2$, all in units of R_E. The vertical cyan and yellow lines in all panels shows where Cassini passes the Enceladus geometrical edge. This is shown in Fig. 7 and marked blue where $z=1$ and $z=-1$ (dark green trajectory crossing the blue dashed lines) and marked in yellow where $R = \sqrt{\hat{x}^2 + \hat{y}^2} = 1$ (light and dark green trajectory crossing the yellow dashed lines).

Figs. 3 and 4 display observations made during flybys E3 and E5, both of which were high inclination flybys. These two flybys took place on 12 March 2008 and 9 October 2008, respectively. We will later contrast these observations with those made on flybys E14 and E18, shown in Figs. 5 and 6, which took place on 1 October 2011 and 14 April 2012, respectively, and were instead approximately parallel to Enceladus' equator, passing from the upstream anti-Saturn side of the moon to the opposite quadrant. In each figure, we discern several distinct plasma regions, delimited by the vertical gray lines, and labeled 'M' for the magnetosphere, 'DT' for the dust trail, 'P' for the plume and 'Ed' for the edge of the plume. In the following sections observations in each region are discussed.

3.2. Dust trail

Firstly, we draw attention to the region encountered downstream of Enceladus on the inbound segments of flybys E3 and E5, during which a strong electron density depletion can be seen from the data shown in panel (a) of Figs. 3 and 4. The electron density reported both from the LP sweeps, and the higher cadence measurements from the 20 Hz data both show depletions in electron density by more than one order of magnitude, while the corresponding ion density remains approximately constant.

This relative depletion in electron density is also characteristic for the plume itself, also encountered on these two flybys following the passage through the dust trail. This discrepancy between electron and ion densities for these particular flybys in the plume region has already been shown by, e.g., by Morooka et al. (2011), Shafiq et al. (2011) and Farrell et al. (2010). The electron density decreases to less
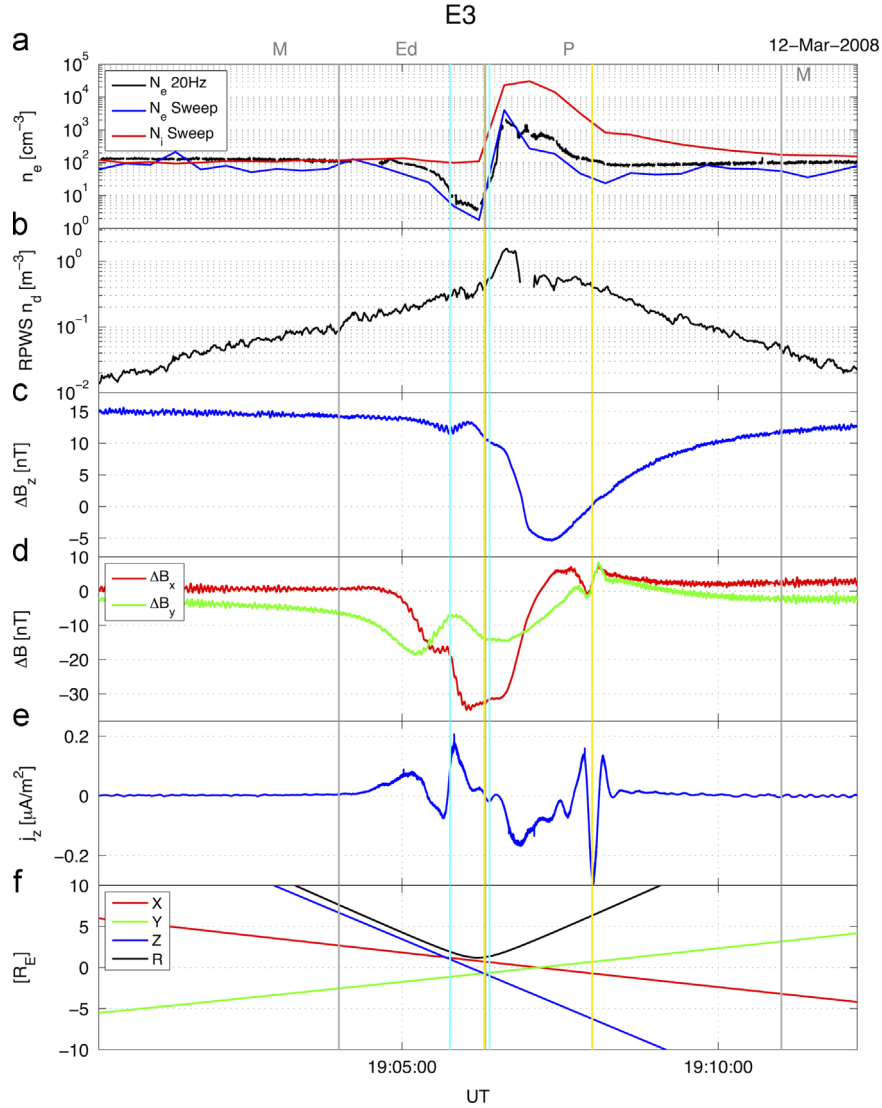
Fig. 3. Time series data for flyby E3. Panel (a) displays the thermal plasma densities; electron density (black and blue) and ion density (red). A discrepancy between electron and ion density of about two orders of magnitude is observed in the trail region (DT), as well as in the plume. This is an indication for electron attachment to dust particles. Panels (b) and (c) show the residual magnetic field, ΔB, around Enceladus where Saturn's magnetic field has been subtracted from the data. The z-component only shows a small change while the x and y component change by about 35 nT and 20 nT, respectively. Panel (d) shows the inferred field-aligned currents, j_z. The main feature here is the southward directed current at Enceladus' geometrical upstream edge (right yellow line). The southward current inside the plume is dominated by parallel currents. The overlaid gray lines give an approximate position of regions around Enceladus, where M is the magnetosphere, DT the dust trail, P the plume and E the edge of the plume. The cyan and yellow lines in all panels indicates where Cassini passes Enceladus' edge. This is marked blue where $z = 1$ and $z = -1$ and marked in yellow where $R = 1$. (For interpretation of the references to color in this figure caption, the reader is referred to the web version of this paper.)

than 10 cm^{-3} in the dust trail region as detected during the four high inclination flybys and the discrepancy with the ion density is about 1–2 orders of magnitude. The onset of electron depletion, and discrepancy with the ion density, starts already at 3–5 R$_E$ north from the Enceladus equatorial plane, and increases steadily. We note that two northern flybys (E12 and E13) show an electron density decrease to below 20 and 50 cm^{-3}, respectively (data shown in overview format in Figs. 8–10). Quasineutrality must hold in a plasma and these data therefore strongly suggest that otherwise free electrons are attached to dust grains ($n_i = n_e + \sum_k Z_{dk} n_{dk}$, where k is a sum over different dust sizes). The discrepancy between the electron and ion density gives a total charge density for the dust distribution of 50–100 cm^{-3} in the dust trail. The electron density is seen to decrease relative to the ion density when dust particles of larger than 1 micrometer (Figs. 3–6, panel b) themselves reach a density of $\sim$0.1 m^{-3}.

Turning now to the measured magnetic fields during these passages, in the trail region ('DT' in Figs. 3 and 4) the ΔB_z field component shown in panel (c) varies little and is at most $\sim$5 nT different from the nominal value upstream, considering all flybys through this region. Meanwhile, clear rotations of the transverse field (ΔB_x and ΔB_y) components are seen in panels (d) of Figs. 3 and 4. This clearly indicates the presence of an approximately field-aligned current flowing within or close to this region ($\sim$19:05 UT), as seen when explicitly estimated using the technique described in Section 2.3 and plotted in panel (e) of these figures. These northward currents have magnitude values of $\sim$0.1 µAm^{-2}. Closer to the moon, we see a northward current (positive j_z) of 0.2 µAm^{-2} in flyby E3 just to the right of the Enceladus limb (left cyan line, $\sim$19:06 UT, Fig. 3) which goes to zero as Cassini approaches the plume. This feature of an northward current is not detected in flyby E5 (Fig. 4).
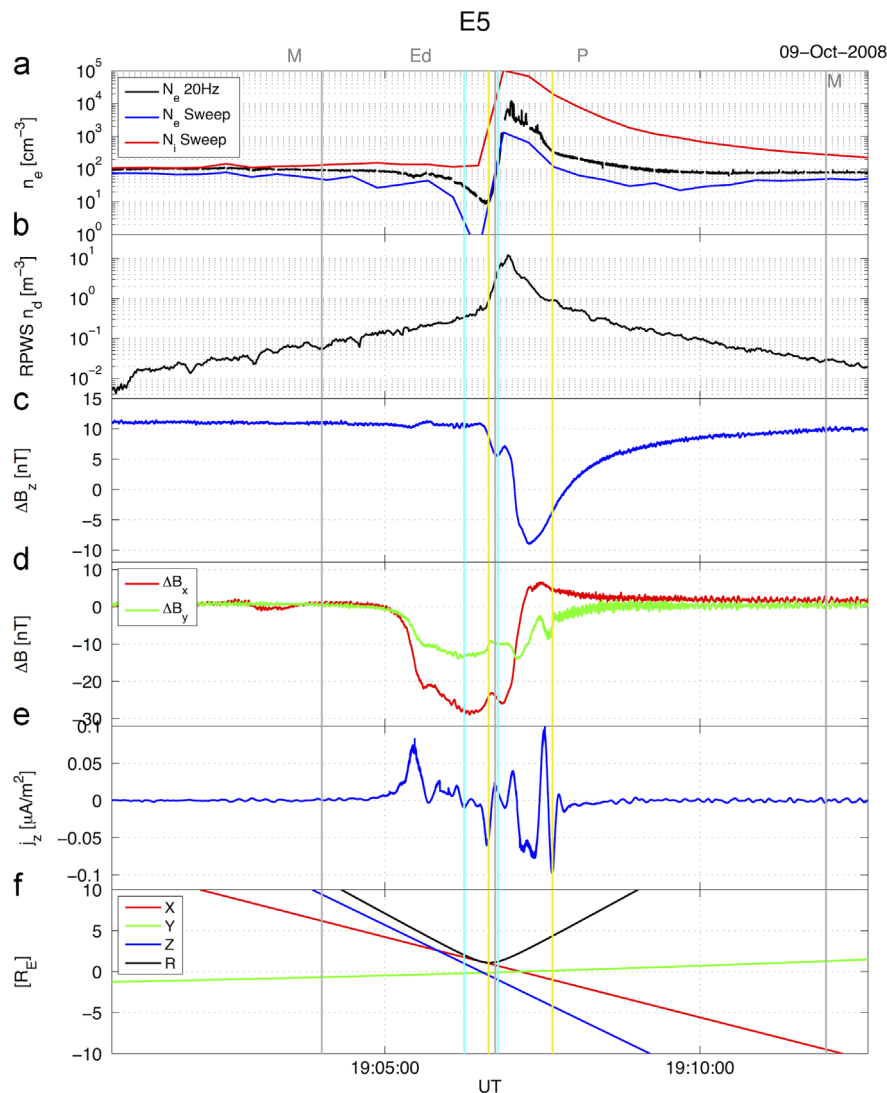
Fig. 4. Time series data for flyby E5 with the same panel layout as in Fig. 3. The geometry and the signatures are similar as for flyby E3, Fig. 3. (For interpretation of the references to color in this figure caption, the reader is referred to the web version of this paper.)

3.3. Plume region

The plume region is a region of overall increased plasma densities (both ion and electron) above the upstream values, as a direct consequence of the local ionization of the neutral gas and dust ejecta. The major properties of this region have been extensively studied and discussed elsewhere, as detailed in the Introduction. For completeness, we here briefly summarize the observations in this region. The electron density increases up to maximum values of $\sim 10^3 - 10^4$ cm^{-3} inside the plume and the ion densities up to $\sim 10^5$ cm^{-3}. The discrepancy between electron and ion density is therefore ~ 2 orders of magnitude, again interpreted as being due to the presence of a significant negatively charged dust population. Meanwhile, the independently measured density of micron sized dust reaches its peak on each flyby at the same location (panel (b) in Figs. 3–6).

In marked contrast to the dust trail region described above, within the plume crossing the ΔB_z component (shown in panel (c) of Figs. 3 and 4) departs 15–20 nT from the background values. The spatial gradient of ΔB_z is most evident within the presented data for E3 and E5, but can also be seen to a smaller extent during E14 and E18. The variation of the ΔB_z is most likely due to the presence of a significant perpendicular current, carried through the plume, due to the deformation of the inflowing magnetic field

and magnetospheric plasma, as it encounters the stationary conductive plume. As a direct consequence, we fully expect that the assumption made in approximating the field-aligned current density is likely violated within the passage of the spacecraft through the plume, and the corresponding data shown in these short segments in panel (e) of Figs. 3–6 should be essentially ignored. Any field-aligned component to the total current in this region is likely much smaller than the perpendicular current, the magnitude of which can be estimated through

$$j_\perp \sim \frac{1}{\mu_o} \frac{\Delta B_z}{\Delta l} \tag{10}$$

where $\Delta l = \sqrt{(\Delta x)^2 + (\Delta y)^2}$ is a distance perpendicular to B_z. The perpendicular magnetic field changes between 10 and 15 nT during a horizontal distance of about half an Enceladus radius ($=126$ km). This results in a current of 0.05–0.1 µAm^{-2}. Such a value is of the order of the field-aligned currents estimated at other locations in the Enceladus plasma interaction, again strongly suggesting that the assumptions used in deriving the field-aligned currents are no longer valid here in the plume region, and is a result of perpendicular currents across the plume.
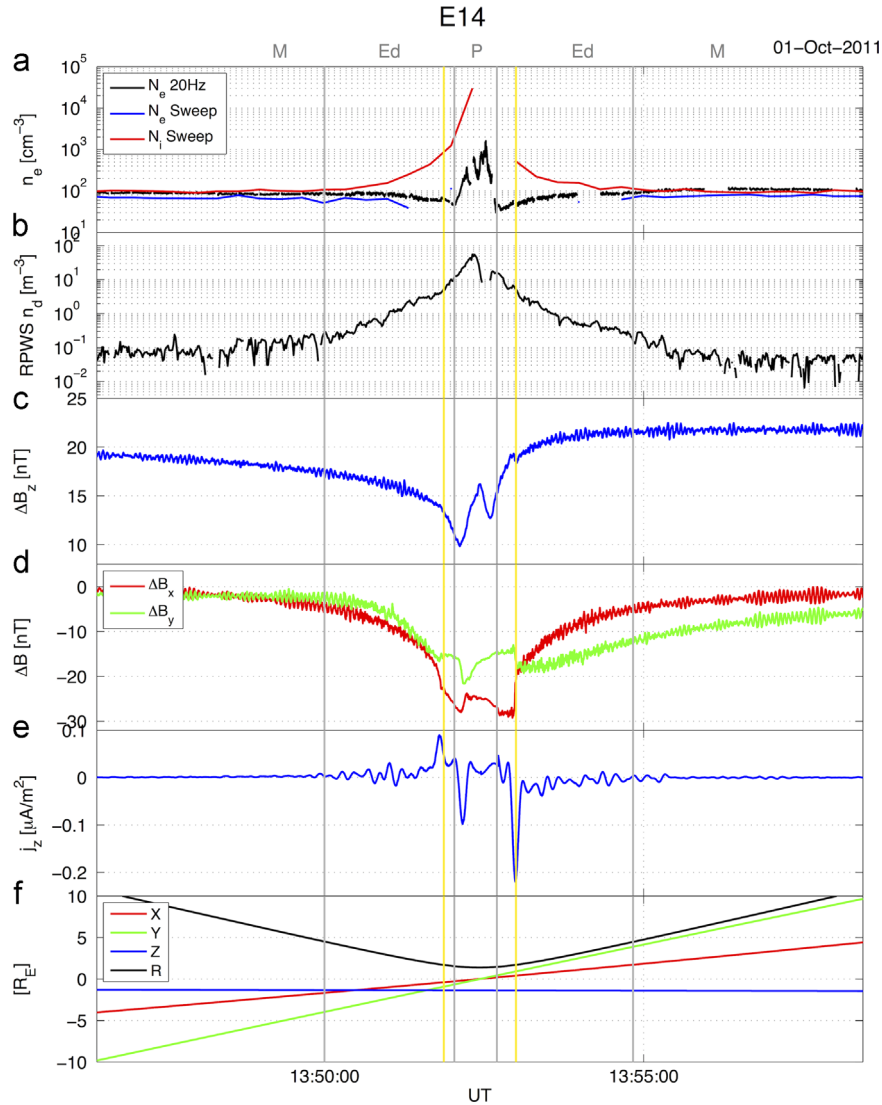
Fig. 5. Time series data for flyby E14 with the same panel layout as in Fig. 3. In the edge region (Ed) an electron density depletion is observed whereas the ion density as well as the micron dust density (panel(b)) already increase. At the downstream geometrical edge of Enceladus, a strong southward current is observed. (For interpretation of the references to color in this figure caption, the reader is referred to the web version of this paper.)

3.4. Plume edge

Figs. 5 and 6 show flybys E14 and E18, which pass close to Enceladus through the plume parallel to the equatorial plane. In contrast to the inclined flybys shown previously, here the electron density shown in panel (a) is seen to decrease in the edge region (marked as 'Ed'), before increasing by several orders of magnitude as the spacecraft encounters the plume (situated between the edge 'Ed' regions). Again, this electron density depletion relative to the ion density is observed in both the LP sweep-derived density, and the 20 Hz measurements. The electron density depletion in the upstream edge region reaches minimum values of 40–50 cm^{-3} and on the downstream edge of the plume down to $\sim$30 cm^{-3} (a drop of $\sim$50–70% compared to the background field). The ion density inferred by the LP sweep is seen to rise within the plume edge region, which again results in a growing discrepancy between electron and ion density. This discrepancy between the electron and ion density is up to 1–2 orders of magnitude. There is no significant difference detected between n_i and n_e in the magnetosphere (upstream) region.

In the plume edge region the magnetic field magnitude changes gradually in all three components (see panels (c) and (d)).

Inside the plume region the largest variations are noticed in the z-component of the magnetic field whereas the x and y magnetic field components are relatively constant.

Close to the downstream geometrical edge of Enceladus (right yellow line in Figs. 5 and 6) is a narrow southward directed current, $\sim$0.2–0.3 μAm^{-2}, in both E14 and E18, as well as a northward directed current at the upstream geometrical edge (left yellow line) of $\sim$0.1 μAm^{-2}. In E3 and E5 (Figs. 3 and 4) there is a current at the upstream geometrical edge (right yellow line) of about 0.1–0.3 μAm^{-2}. Flyby E5 shows a small (about 0.05 μAm^{-2}) southward directed current at the downstream geometrical edge (left yellow line, Fig. 4) that E3 does not show. In the magnetosphere and outside of the plume there are no indications of magnetic field-aligned currents of comparable strength.

4. Observations from all 20 flybys

In this section we show all, except one, available flybys up to 2013 in planar $\hat{x} - \hat{z}$ coordinates. Flyby E11 is out of bounds of the figure, with a closest approach altitude of 12R_E south. The electron density, n_e, is shown in Fig. 8(a) and the total magnetic field, B_{tot},
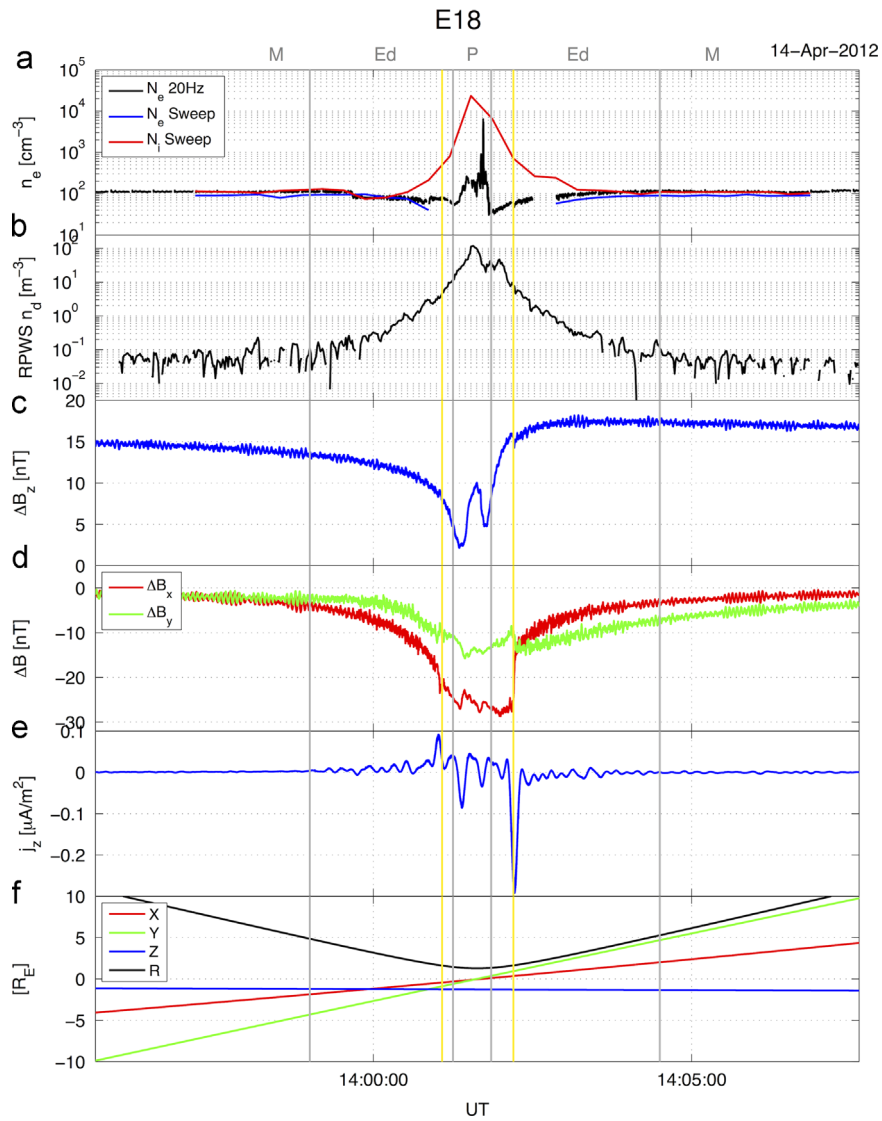
Fig. 6. Time series data for flyby E18 with the same panel layout as in Fig. 3. The geometry and the signatures are similar as for flyby E14, Fig. 5. (For interpretation of the references to color in this figure caption, the reader is referred to the web version of this paper.)
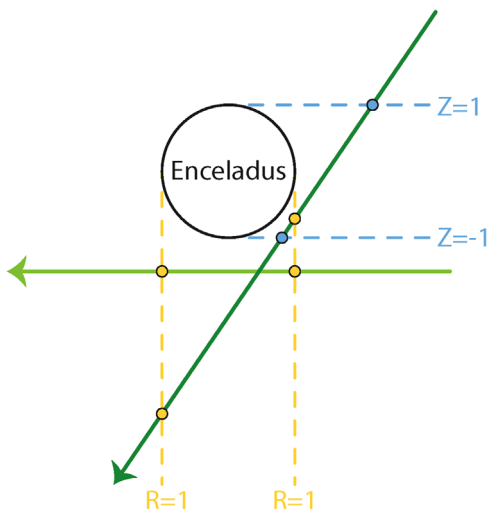

Fig. 7. The position of Cassini with respect to Enceladus' edge is indicated by the cyan and/or yellow lines in Figs. 3–6. Enceladus' edge is marked blue where $z=1$ and $z=-1$ (green line crossing blue dashed line) and yellow when $R=\sqrt{\hat{x}^2+\hat{y}^2}=1$ (green line crossing yellow dashed line). (For interpretation of the references to color in this figure caption, the reader is referred to the web version of this paper.)

in Fig. 8(b). Two distinct regions of interest are noticeable; the plume region and the Enceladus trail region. The plume region can clearly be detected as an enhancement in both electron density and magnetic field, here visible as the red/orange/yellow parts of the flybys. The electron density increases more than two orders of magnitude compared to the surrounding magnetospheric density. The magnetic field measurements (Fig. 8(b)) show an enhancement by $\delta B > 20$ nT in the plume region. This is interpreted as a magnetic field pile-up and draping around the plume region caused by slowing of the magnetospheric plasma flow and creating an induced magnetosphere around the plume.

The Enceladus trail region shows an electron density decrease (blue colored flybys, Fig. 8(a)) downstream of Enceladus, as detected during the four high inclination flybys (E3-E6). Here the data show a density decrease in both the northern flybys (E12, E13) that can be part of the Enceladus trail region. The trail region is broader in the $\hat{z}$−direction than Enceladus itself, and the electron density decrease is significant already at $3–5R_E$ north of the equatorial plane (Fig. 8(a)). The magnetic field magnitude (Fig. 8(b)) in the trail region is not significantly affected and shows typical upstream values.
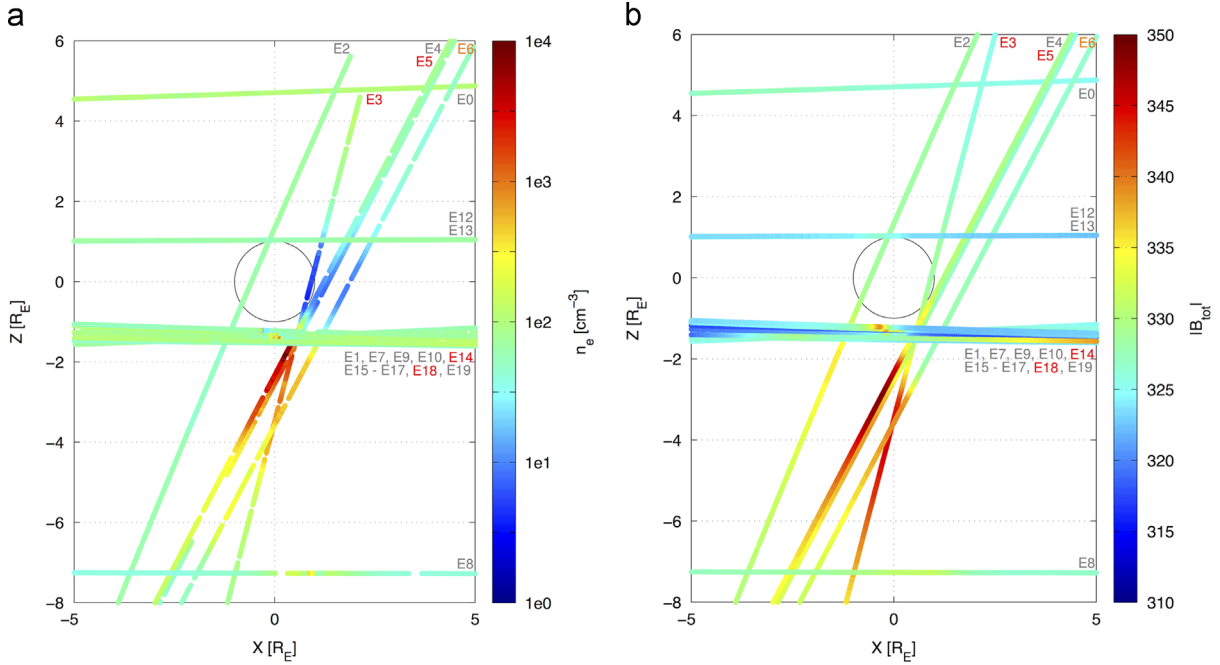
Fig. 8. Enceladus' flybys in planar $\hat{x}-\hat{z}$ coordinates. The color scale indicates the electron density in (a) and the total magnetic field corrected for Saturn's dipole field in (b). The corresponding Enceladus flybys are indicated. The plume is clearly visible in both the electron density as well as the magnetic field as a pile up (reddish parts of the flybys). The trail region is seen as en electron depletion region (blueish parts of the high inclination flybys) to extend north up to 3–4 R_E. The magnetic field however does not change drastically there. (a) n_e. (b) B_{tot}. (For interpretation of the references to color in this figure caption, the reader is referred to the web version of this paper.)
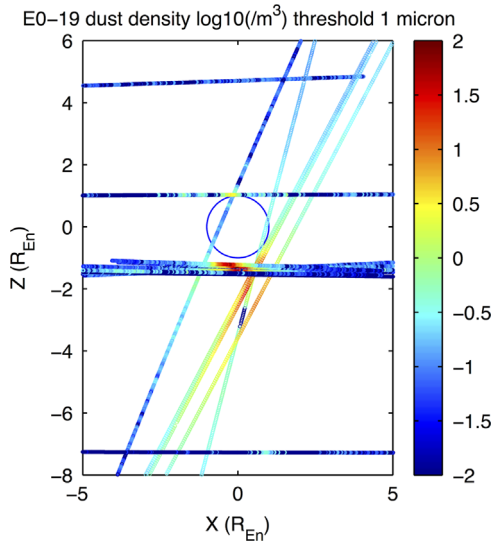

Fig. 9. Enceladus' flybys in planar $\hat{x}-\hat{z}$ coordinates. The color scale indicates the dust density from the RPWS/WBR. The dust density increases inside the plume region and decreases in the trail region. (For interpretation of the references to color in this figure caption, the reader is referred to the web version of this paper.)

Additionally we show the RPWS micron sized dust measurements in Fig. 9. Observing a clear density increase in the plume region which also appears in the trail region, although less prominent (cyan color of flybys E3-E6). This result may be due to the general increase of the E-ring dust density toward the equatorial plane or due to secondary impact ejecta from the surface Spahn et al., 2006. The flyby coverage near the equatorial plane does not allow a definite conclusion from the present data.

Fig. 10 shows the derived field-aligned currents. Some flybys have been displaced by a small value so that flybys with similar geometries are clearly visible in the plots, see figure caption. Inside the plume region a southward directed current is seen in all 4 representations of the same data. These currents are most probably dominated by perpendicular currents and show up as apparent field-aligned currents in the calculation (E3-E6). In the northern (3–4 R_E), downstream and anti-Saturn direction northward currents are observed. These currents can be part of an Alfvén wing current system (Section 5.3). In the downstream direction of Enceladus there are southward currents visible in flybys E4 and E5. Along the limb of Enceladus ($\hat{y}-\hat{z}$ projection, black vertical lines) are strong currents that are directed southward on the Saturn side and northward on the anti-Saturn side. These are field-aligned currents. In the $\hat{x}-\hat{z}$ projection we see that these currents are in no specific pattern in the plume region. Overall small currents are directed south towards Saturn ($+\hat{y}$) and north away from Saturn ($-\hat{y}$).

5. Discussion

In this paper we have studied field and particle data from multiple sensors on two Cassini instruments, obtained on all Enceladus flybys conducted to date.[1] Here, we briefly summarize our results and comment on their wider implications.

5.1. Plasma regions surrounding Enceladus

From the RPWS Langmuir probe data as well as from the MAG magnetometer and the RPWS electric antenna data from the wideband receiver we can clearly distinguish several distinct plasma regions around Enceladus. Specifically, in addition to the widely reported dusty plume present over Enceladus' south pole, we also show that a distinct boundary layer to this plume is encountered on those flybys that traverse the plume perpendicular to the upstream plasma flow direction. Significantly, detailed analysis of data from the Langmuir probe shows the presence of a dust trail forming downstream of Enceladus. This is not a wake in

---

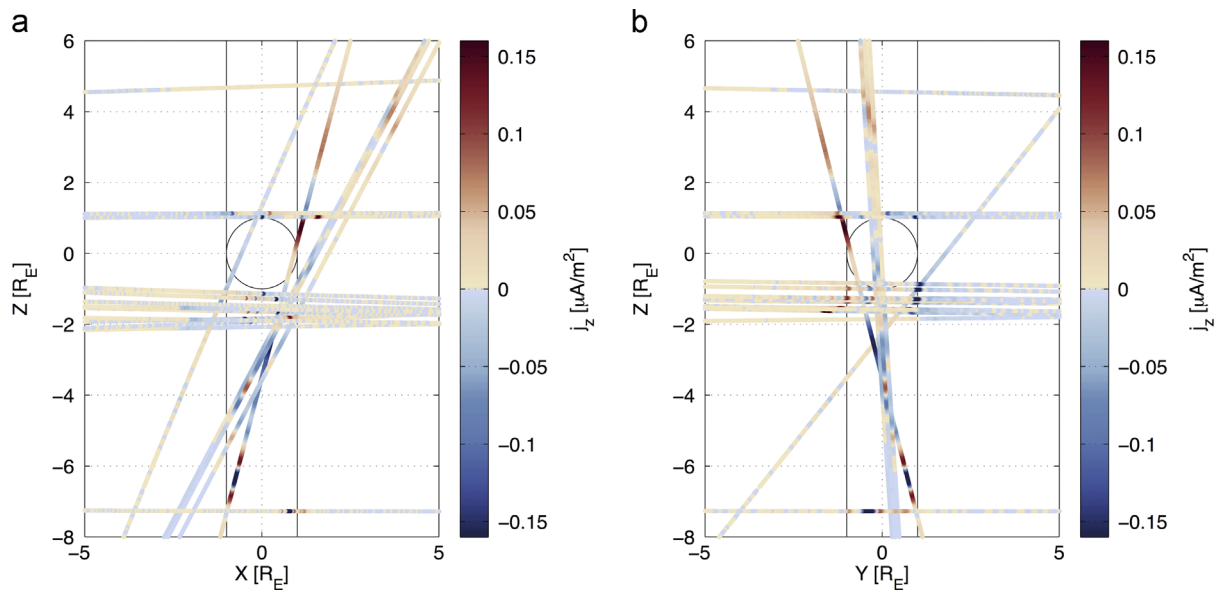[1] May 2015.

Fig. 10. Current along Enceladus' flybys in planar $\hat{x} - \hat{z}$ (a) and $\hat{y} - \hat{z}$ (b) presentation, where flybys of similar geometry have been moved slightly to be visible (horizontal flybys E1, E7, E9, E10, E12-16, E18 and E19 as well as high inclination flybys E4 and E5). There is no symmetry along the magnetospheric flow direction ($\hat{x}$), (a), but along the Enceladus – Saturn direction ($\hat{y}$), (b), where currents are generally southward on the Saturn facing side of Enceladus and northward away from Saturn. (For interpretation of the references to color in this figure caption, the reader is referred to the web version of this paper.)

the classical sense where the wake is depleted of ions when the upstream flow speed is larger than the thermal speed. However, in the trail we observe a dropout of electron density and constant ion density. Another reason why this is not a trailing plasma wake is that the electron dropout region is extended north by 2–4 R_E.

Each of these large-scale plasma regions identified are shown in the illustration in Fig. 11 embedded in Saturn's circulating magnetospheric plasma. We now briefly summarize their properties.

(1) The Enceladus plume, in which LP measurements show localized increases in both ion and electron density, but with a significant excess density of ions, indicating that a significant amount of negatively charged dust is also present. Dust particles are individually charged to the point where they reach equilibrium with the surrounding plasma potential. The observed density of dust grains larger than 1 μm obtained from the RPWS WBR receiver inside the plume range from 1 to 100 particles/m^3 (see Section 5.2). We infer the smallest dust particles to be of the order of 1 nm in size from the RPWS observations inside the plume (see below), consistent with earlier reported CAPS observations (Hill et al., 2012), and assuming that the simple power law size distribution of the micron-sized charged dust measured by RPWS extends to the smaller nanometer sized particles. The inferred mass density range of all dust in the plume amounts to 10^{-14}–10^{-11} kg m^{-3}, the larger values existing closer to the plume center.

(2) The broad "edge region" or plume boundary, in which a depletion in the magnetospheric electron density is observed, is likely the result of their attachment to dust particles.

(3) The dust trail, in which we measure a strong electron depletion while the ion density stays more or less constant. Here, again, a large fraction of the electrons are collected by dust particles. Such an effect could be due to an enhancement in the E-ring dust density in the wake of Enceladus. Whether this effect is due to a true trail enhancement of dust or an enhancement of the E-ring near the equatorial plane is not clear from the available data analyzed in this paper, since there was only one upstream flyby, E2, in which no evidence of a significant electron density depletion relative to the ions was detected. Finally, we note that (with the observations available), no evidence is present for significant
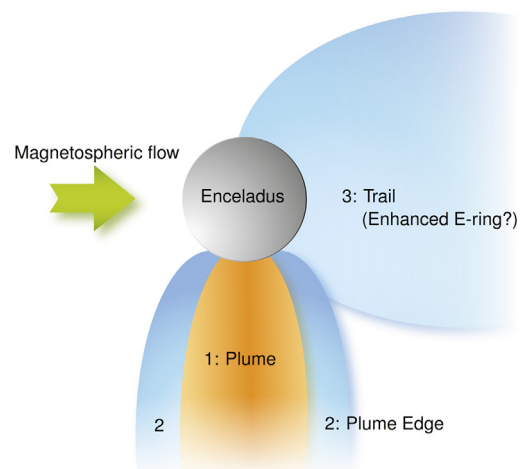

Fig. 11. An illustration of the plasma regions studied in this paper, not to scale. Identified regions in the electron density measurements, numbered for convenience. The green arrow shows the direction of the magnetospheric plasma flow. Region 1 depicts the plume region, and region 2 its edge. Region 3 is the dust trail region. The colors give an electron density increase (orange) or electron density decrease (blue) in the respective areas. (For interpretation of the references to color in this figure caption, the reader is referred to the web version of this paper.)

variations, from flyby to flyby, in either the plasma properties of any of these structures or their physical extent.

5.2. Properties of dust populations

Here, we explore the relationship between the discrepancy between ion and electron densities (as measured by the Langmuir probe) and the partial dust density (as measured on the WBR). We remind the reader that these two measurements are made entirely independently of each other with different sensors and different receivers.

It has been found that the dust grain size distribution around Enceladus obeys a power law (e.g., Kempf et al., 2008; Kurth et al.,

2006; Ye et al., 2014), which is consistent with other observational cases (e.g., Yaroshenko et al., 2009; Wahlund et al., 2009; Shafiq et al., 2011). The dust distribution can therefore be written in the following form:

$$n_d(r_d) \propto r_d^{-\mu} \quad \text{where } \mu \approx 4-5, \tag{11}$$

where n_d and r_d are the dust density and dust grain size, respectively. The grain differential number density is therefore given by

$$n_d(r_d) \, dr_d = n_1 \left(\frac{r_1}{r_d}\right)^\mu dr_d, \tag{12}$$

where n_1 is the differential number density for dust grains of $r_1 = 1 \, \mu m$ radius and is used for normalization (Shafiq et al., 2011). From the RPWS dust measurements we derive the total number density of particles larger than $r_1 = 1 \, \mu m$, given by

$$n_{d,tot}(>r_1) = \int_{r_1}^\infty n_d(r_d) \, dr_d = n_1 r_1^\mu \int_{r_1}^\infty r_d^{-\mu} \, dr_d = \frac{n_1 r_1^\mu}{1-\mu} \left[r_d^{\mu-1} \right]_{r_1}^\infty \tag{13}$$

Noting that the upper limit goes to zero, it can be shown that

$$\lim_{r_d \to \infty} r_d^{1-\mu} = 0, \tag{14}$$

resulting in total number density for grains larger than $1 \, \mu m$ as

$$n_{d,tot}(>r_1) = -\frac{n_1 r_1}{1-\mu} \tag{15}$$

The total net charge on a dust population can be found through

$$e(n_i - n_e) = \int_{r_{min}}^\infty q_d(r_d) n_d(r_d) \, dr_d \tag{16}$$

Using the expression presented by Horányi et al. (2004) we can estimate the grain charge in equilibrium with the surrounding plasma as

$$q_d = -\alpha 4\pi\epsilon_0 r_d \Phi_f \tag{17}$$

where q_d and r_d are the dust charge and size, respectively, ϵ_0 is the vacuum permittivity, α is a proportionality factor which is a function of the ion mass m_i and is about 3.66 for water group ions (Horányi et al., 2004; Shafiq et al., 2011), and Φ_f the grain surface potential which can be approximated by the spacecraft potential, U_{SC}. The expression for the net charge becomes

$$n_i - n_e = \left(\frac{4\pi\epsilon_0 \alpha U_{SC}}{e}\right) \frac{n_1 r_1^\mu}{(2-\mu)} \frac{1}{r_{min}^{\mu-2}} \tag{18}$$

Substituting n_1 with the equation from (15) into (18) gives the following expression:

$$n_i - n_e = -\left(\frac{4\pi\epsilon_0 \alpha U_{SC}}{e}\right) \frac{(1-\mu)}{(2-\mu)} r_1^{\mu-1} \frac{1}{r_{min}^{\mu-2}} n_{d,tot}(>r_1) \tag{19}$$

This equation therefore explicitly relates the two independently measured quantities, the differential density, $n_i - n_e$, and the total dust density for particles larger than $1 \, \mu m$, $n_{d,tot}$.

In Fig. 12 we show the differential charge density versus the dust density around Enceladus. The vertical axis shows the measured charge density difference between ion and electron density from the Langmuir probe in cm^{-3} versus the total dust density larger than $1 \, \mu m$ sized dust from the RPWS wideband receiver in m^{-3} on the horizontal axis. For the difference in densities both sweep and 20 Hz data were used for determining the electron density (depending on data coverage) and sweep data for the ion density. The individual measurements are shown color-coded, where the plume is represented by the high inclination flybys E3 (red) and E5 and E6 (green) as well as E14 (black left) and E18 (black right). Flyby E3 had a different geometry than flybys E5 and E6. For the E14 flyby we did not have complete ion data and therefore the differential density is most probably underestimated. Data from the plume edge region is obtained from flybys E14 and E18 (orange) and the trail region by the high inclination flybys E3,
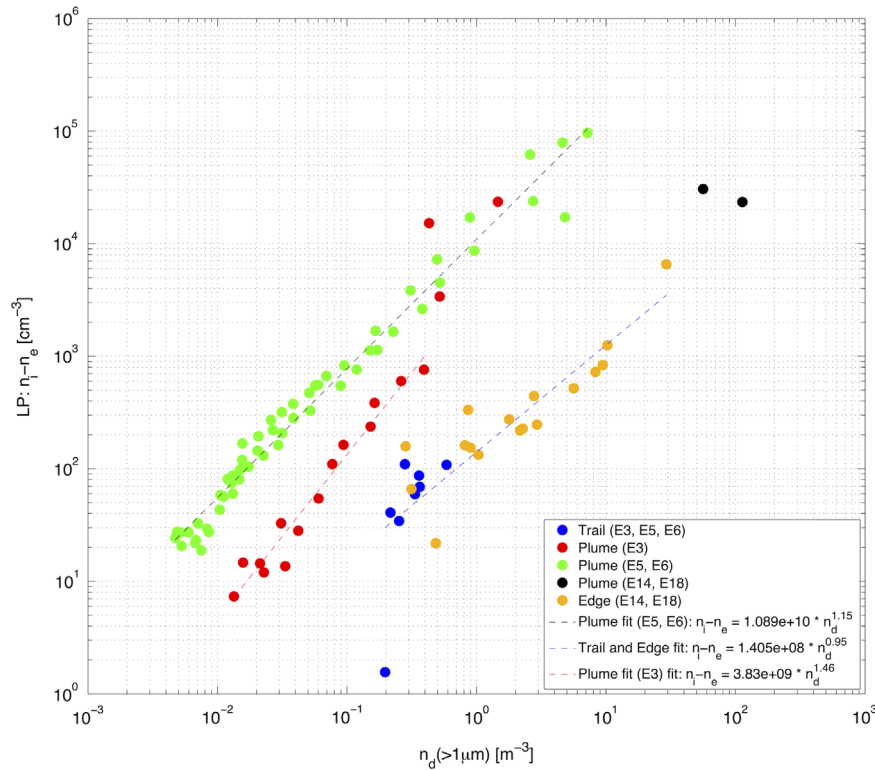

Fig. 12. Charged dust density ($n_i - n_e$) dependence on dust density of particles $> 1 \, \mu m$. The data is separated into the different regions. The plume is represented with data from the high inclination flybys E3 (red) and E5 and E6 (green) as well as E14 (left-) and E18 (right black data point). The trail (blue) is determined by flybys E3, E5 and E6, and the plume edge region (orange) by E14 and E18. The fit to the plume edge and trail, and the plume data shows an approximate linear relationship. (For interpretation of the references to color in this figure caption, the reader is referred to the web version of this paper.)

Table 2
List of minimum grain sizes in the plume region, and the edge and trail region, for specific μ.

μ	Plume $r_{\min}$ (m)	Edge/tail $r_{\min}$ (m)
3	2×10^{-12}	120×10^{-12}
4	1×10^{-09}	8×10^{-09}
5	10×10^{-09}	38×10^{-09}

E5 and E6 (blue). In each region, within the log-log plot, the observations are clearly linearly related, as expected from Eq. (19). We obtain power-law fits to these data by simple polynomial least squares, with the derived fit to the plume data of flybys E5 and E6 (black dashed line) given by

$$n_i - n_e = 1.09 \cdot 10^{10} \cdot n_d(>1\,\mu m)^{1.15}, \tag{20}$$

and the plume fit to flyby E3 (red dashed line) given by

$$n_i - n_e = 3.83 \cdot 10^{9} \cdot n_d(>1\,\mu m)^{1.46}. \tag{21}$$

Meanwhile, the derived fit to the edge and trail data (blue dashed line) is given by

$$n_i - n_e = 1.405 \cdot 10^{8} \cdot n_d(>1\mu m)^{0.95}. \tag{22}$$

From these fits we see an approximate linear relationship (unit exponent) between charge density difference and dust density. This indicates that the Horányi et al. (2004) charging relation, Eq. (17), for dust in equilibrium with the surrounding plasma can be used to determine the grain potential. Hence, the dust distribution can be described as a power law with exponent μ. In addition, Fig. 12 empirically verifies the consistency of the two independent RPWS dust density measurements.

The relationship in Fig. 12 is particularly interesting to compare to a recent study by Yaroshenko et al. (2014), in which several particle-in-cell simulations of the electron, ion and dust densities around a spherical probe taken to represent Cassini were presented. For the densest plume region, their estimates indicate that the difference between ion and electron densities observed by the LP would also be correspondingly large, in line with the interpretation of LP data used by us and Morooka et al. (2011). However, they also suggested that outside this region, the observed difference between n_i and n_e may instead be a manifestation of the inhomogeneous plasma structure around the spacecraft, particularly the decrease of electron density at the probe due to the repelling potential field when the spacecraft is negatively charged. This model result is not easily reconciled with the data in Fig. 12, as there is no reason why spacecraft sheath effects should scale with the density of grains larger than 1 μm derived independently from RPWS wave measurements by the method of Ye et al. (2014). We therefore conclude that while the spacecraft sheath effects pointed to by Yaroshenko et al. (2014) certainly need to be considered, they do not dominate the Enceladus measurements and have little impact on our results.

The recently published numerical models by Meier et al. (2014) and Kriegel et al. (2014) attempt to theoretically infer the detailed dust size distribution below a size of 10 nm. Reasonable fits to the nanometer sized grain observations by Hill et al. (2012) are indeed achieved by Meier et al. (2014) within the plume region, but significant differences remain especially just outside the central plume region. This discrepancy is likely due to the treatment of the nanometer sized charged dust grains as individual particles influenced by electric fields induced by the rest of the plasma environment rather than a collective ensemble. We recognize that such a power law cannot extend all the way down to the smallest dust sizes, as is evident in the CAPS nanometer sized grain observations by Hill et al. (2012). They show dust number densities of a few $1000\ cm^{-3}$. A break of the power law needs occur slightly above 10 nm grain sizes in order to be consistent with the CAPS observations. This does not alter our observational result that the total charge density on the dust is approximately proportional to the number density of micron sized dust presented in Fig. 12, and that these data can be fitted to high precision with a power law. However, the exact dust distribution near the moon Enceladus needs further study.

In Fig. 12 there is a difference between the plume region and the trail and plume edge data of two orders of magnitude in n_d. The only other variables in Eq. (19) are the spacecraft potential, U_{SC}, the minimum grain size, $r_{\min}$, and μ, the power law exponent. The spacecraft potential is measured by the Langmuir probe and does not change more than a factor of ~ 2 (see for example Fig. 15). Therefore, this cannot account for two orders of magnitude change in n_d. The exponent, μ, is reasonably well constrained to values of 4–5, with some evidence having been presented for the steepening of this distribution on flybys closer to the plume base (e.g., Kurth et al., 2006; Kempf et al., 2008). Thus by using Eq. (19) we can estimate the size of the smallest particles by solving for $r_{\min}$, with $\alpha = 3.66$ and $U_{SC} = -2$. Table 2 shows the result on the minimum dust grain size using different μ. For $\mu = 3$ the minimum dust grain size calculated in the different regions are smaller than water molecules which is clearly unreasonable. Substituting $\mu = 5$ yields the smallest grains in the plume to be of the order of 10 nm in radius. Hill et al. (2012) reported particle size estimates down to 1 nm, which corresponds to $\mu = 4$. Therefore, the results are consistent with a power law dust size distribution which is charged to equilibrium with the surrounding plasma. We note that while the RPWS dust density (n_d) measurements are correlated with our measurements of the differential charge density ($n_i - n_e$) most of the electrons are likely bound to the smaller rather than the larger grains.

In summary, an electron density depletion is observed in the downstream region. Although the coverage is scarce, flybys E1, E10, E13 and E16 show no signature of an electron depletion in the upstream region (Fig. 8(a)). The Enceladus plasma interaction is influenced by charged dust and dust dynamics. Magnetospheric plasma slowdown has also been observed in the northern hemisphere of Enceladus which suggests a charged dust pick-up current (Farrell et al., 2012). Inside the plume the densities of electron, ions and dust increase by more than two orders of magnitude. The dust pick-up current is supposed to be $< 15\%$ of the ion pick-up current and constitutes to a change in the magnetic field of a few nT (Farrell et al., 2014). Free electrons are again collected by the dust within the plume edge region. The electron density decreases while the ion density increases which results in an approximate charged dust density, $Z_d n_d$, of about $10^3\ cm^{-3}$.

5.3. Current systems and the Alfvén wings

We briefly comment on the presented estimates of the field-aligned current density obtained from magnetometer, and their relationships to the various plasma regions seen around Enceladus. Firstly, we note the clear presence of the field-aligned currents on each side of the moon forming the Alfvén wing structure, first described for Jupiter's moon Io by Ness et al. (1979) and Neubauer (1980).

From the measurements presented in Fig. 10(b), where we have a general sign reversal from positive (northward directed) to negative (southward directed) currents density taking place with the transition from $-\hat{y}$ to $+\hat{y}$ coordinates towards Saturn. We note more intense localized currents associated with the geometrical edge of the moon, with the same organization in their sign, northward away from Saturn and southward on the Saturn facing side. These agree with previous related studies (e.g., Saur

et al., 2007; Simon et al., 2011). The locations of the field-aligned currents are consistent with auroral hiss observations (Gurnett et al., 2011; Leisner et al., 2013). Typical intensities of these currents are also broadly consistent with our estimate of the magnitude of the perpendicular current that couples these two field-aligned currents across the conductive plume "ionosphere". Specifically, we infer typical current densities of the order of 0.1–0.3 μAm^{-2}. As with the main currents of the Alfvén wing structure, we fully expect these currents to ultimately close via Pedersen currents in Saturn's ionosphere.

Larger dust grains with gyroradii greater than the ~100 km length scale of interest will not contribute to the Alfvén wing structure. Meanwhile, the possibility does exist that smaller sized grains with gyroradii smaller than this value do play some role in establishing the structure of the system. However,

given the wide uncertainties and lack of robust measurements across all relevant dust sizes, we are not able to reliably estimate the precise contribution of nanometer grains to the system as a whole.

More importantly, we do not detect evidence for any obvious, stable current system (field-aligned or otherwise) associated with the newly identified dust trail. The absence of such a current system must be interpreted as evidence that the velocity of the neutral material in this region differs little from that of the upstream inflowing plasma, such that no significant acceleration of the newly ionized dust is required for it to reach that of the ambient plasma, meaning that a strong coupling must exist between the charged dust and the rest of the plasma. Similarly, no signature of the passage of the spacecraft through this dust trail is seen in the magnetic field magnitude, shown in Fig. 8(b). Farrell
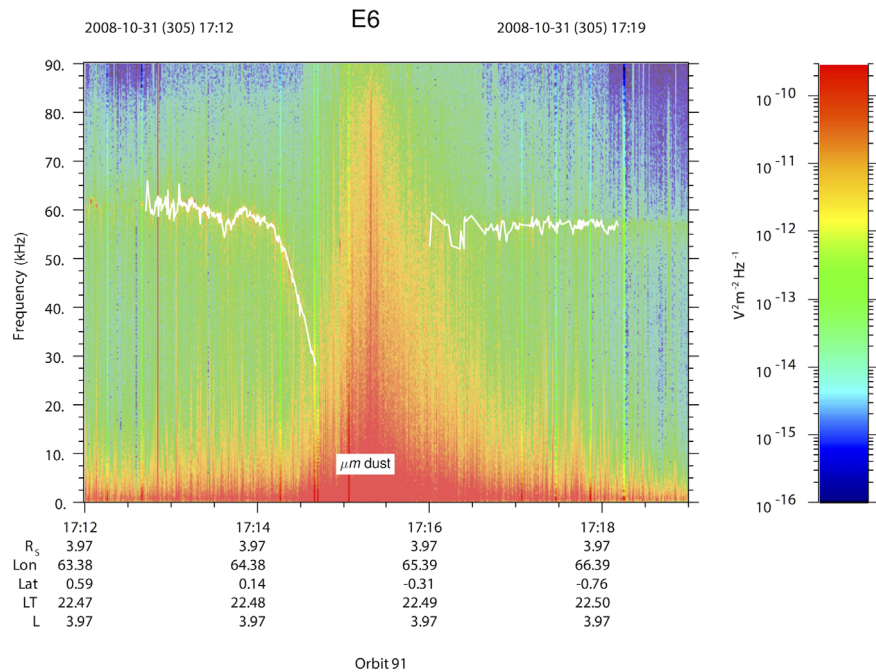

Fig. 13. Electric field data where the white line traces the upper hybrid frequency. There are no data points found between 17:14:30 and 17:16:30 because the measurements are obstructed by micrometer sized dust hits (Wang et al., 2006). The red line (17:12:51 UT) shows the reference time for the slice spectrum used in Fig. 14. (For interpretation of the references to color in this figure caption, the reader is referred to the web version of this paper.)
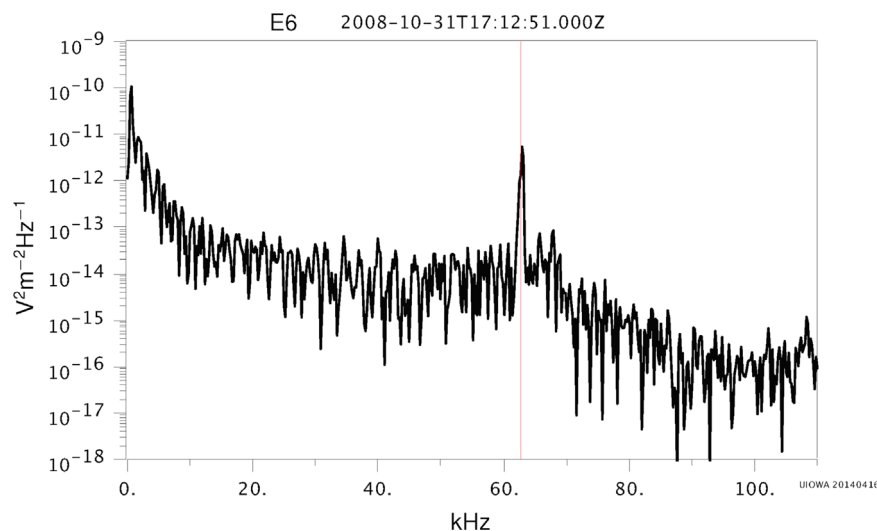

Fig. 14. Vertical slice trough the spectrum in Fig. 13 (red line), to determine the upper hybrid frequency. The horizontal axis gives the frequency [Hz] and the vertical axis the power [V^2 m^{-2} Hz^{-1}]. The upper hybrid frequency peak is at 62.8 kHz (red line). (For interpretation of the references to color in this figure caption, the reader is referred to the web version of this paper.)

et al. (2012) pointed out that a slowdown of the magnetospheric flow is observed in the northern hemisphere which is related to fine dust grains that are accelerated by the Lorentz force. Such a slowdown is also observed directly (Morooka et al., 2011; Wahlund et al., 2005, 2009; Holmberg et al., 2012). They also state that this structure is quasi time-stationary in the frame of Enceladus and only amounts to a few nT change in the magnetic field. However, we again note that the lack of upstream flybys does limit our ability to properly constrain the structure of the dust trail in the azimuthal direction.

6. Conclusions

This paper has investigated the plasma structures around Enceladus. Here, we report the detection of a dust trail, formed downstream of the moon. This is manifested in our observations by a localized depletion in the electron density, likely indicating the attachment of some fraction of the electrons to dust grains within this region. While we tentatively conclude that this region is confined to the down-stream side of the moon, we note that further observations are required before firm conclusions can be
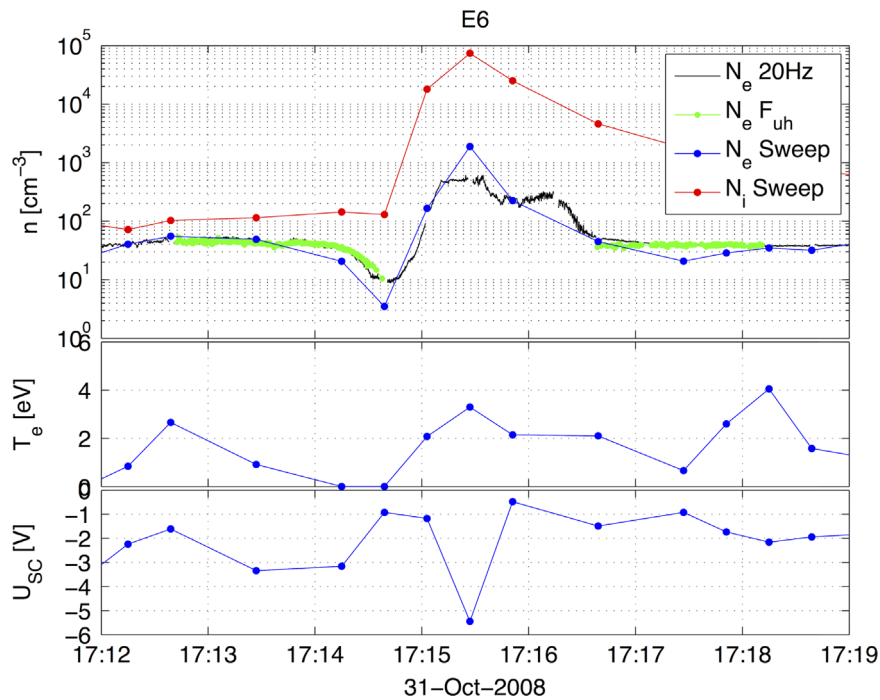

Fig. 15. The top panel displays thermal plasma densities; electron density derived from the constant bias mode, the sweep, and the upper hybrid frequency (black, blue and green), as well as ion density (red) derived from sweeps. The middle panel shows the electron temperature and the bottom panel the spacecraft potential, both derived from sweep analysis. Here the electron temperature and spacecraft potential do change only minimal compared to the orders of magnitude in density. (For interpretation of the references to color in this figure caption, the reader is referred to the web version of this paper.)
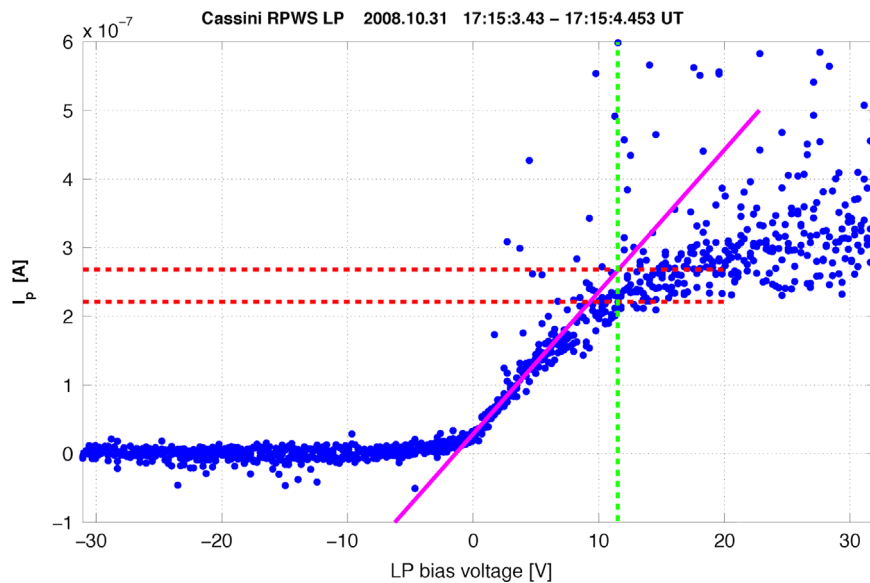

Fig. 16. Example of a sweep inside the dense part of the plume for flyby E6. The magenta solid line approximates the linear part of the sweep curve. The dashed green line shows the bias potential at +11.5 V and the red dashed lines show the difference in current level from the straight line fit at the bias potential, which is about 5 μA. (For interpretation of the references to color in this figure caption, the reader is referred to the web version of this paper.)

reached on its spatial extent. With the available data, both this trail, and indeed the other plasma structures present around Enceladus appear to be stable in time. Importantly, this dust trail has no apparent effect on the total magnetic field strength, indicating that the ambient plasma flow is not significantly slowed by the presence of the material present, presumably because it is already convecting with the E-ring plasma at a slowed speed (compared to corotation) throughout its evolution. The E-ring dust and plasma can therefore be regarded as a collective ensemble moving together (Wahlund et al., 2009).

Furthermore, we have shown that a strong agreement exists between the independent measurements made of the dust density, by comparing observations of the charge density difference from the Langmuir probe, and the density of large (> 1 μm) dust grains seen by the WBR receiver, both of which are part of the RPWS instrument package. The close correspondence between these measurements indicates both that these dust particles are charged such that they reach an equilibrium with the surrounding plasma, and that their size distribution lies within previously published constraints. The consistency with observations by using dust charging in equilibrium with the plasma also gives doubt to that other charging mechanisms of the dust are significant, like triboelectric charging (as suggested by Jones et al., 2009).

Further study of the complex dust–plasma interactions present around Enceladus is clearly required, although the constraints imposed by the limited coverage obtained through the Cassini flybys necessarily limit our understanding of both the spatial extent and the dynamical variations in these structures. We are confident that understanding of the processes operating at Enceladus leading to the formation of these structures is of value to other solar system objects where we expect dust–plasma dynamics to be of significance.

Acknowledgements

Appendix A. Calibration

In the OML limit the current to the probe is proportional to the electron density (see Section 2.1)

$$I_e \propto n_e. \tag{A.1}$$

The spacecraft potential and electron temperature do not vary significantly in order to contribute essentially to the variations of the sampled current, see Appendix C. The LP current therefore needs to be calibrated to plasma densities by some other method. For this purpose we use the upper hybrid frequency sampled by the electric field spectral analyzer, also part of the RPWS. The upper hybrid emission frequency, f_{uh}, is a function of electron plasma density, e.g. (Gurnett et al., 2004; Farrell et al., 2010) according to

$$f_{uh}^2 \simeq f_{ce}^2 + f_{pe}^2 \tag{A.2}$$

and is composed of the cyclotron frequency, f_{ce}, and the plasma frequency, f_{pe}. The magnetic field in the cyclotron frequency, $f_{ce} = qB/m$, is measured with the RPWS magnetic field instrument.

Fig. 13 shows an example of an upper hybrid method for determining the electron density. The Enceladus flyby, E6, is a high inclination flyby (passing Enceladus from north to south, going

through both the trail and the plume region) on the 31st of October 2008. The white line traces the upper hybrid emissions. There are no identifiable emission lines between 17:14:30 UT to 17:16:30 UT. The red vertical line at 17:12:51 UT shows the position used for determining the upper hybrid frequency as shown in Fig. 14.

Using the standard expressions for the plasma frequency ($f_{pe}^2 = n_e e^2/\epsilon_0 m_e$) one arrives at an expression of the electron density by using the upper hybrid and cyclotron frequency

$$n_e = \frac{\epsilon_0 m_e}{e^2}\left(f_{uh}^2 - f_{ce}^2\right) \tag{A.3}$$

This electron density is then used as reference level in the plasma disk.

The fit of the LP continuous 20 Hz current measurements to the upper hybrid derived electron number density is made close to Enceladus in the plasma disk. An example is shown in Fig. 15, top panel. Here the derived electron density from the upper hybrid plasma frequency is shown in green whereas the electron density with an applied calibration factor of $\sim 8.8 \times 10^8$ cm^3/A for the E6 encounter, is shown in black. A discrepancy between the two methods can be detected around 19:17:17 UT. This is due to a dependence of the LP sampled current on the spacecraft potential and or electron temperature and is discussed in Appendix C.

Appendix B. Density derivation from LP sweep measurements

B.1. Electron density

As mentioned before in Section 2.1, the current to a Langmuir probe is given by Eqs. (1)–(3), mentioned here again

$$I_\alpha = \begin{cases} I_{\alpha,o}(1 - \chi_\alpha), & q_\alpha U < 0 \\ I_{\alpha,o}e^{-\chi_\alpha}, & q_\alpha U > 0, \end{cases}$$

The slope of the curve given at positive potential is then given by

$$I_{tot} = n_e e A_{LP}\sqrt{\frac{eT_e\,[eV]}{2\pi m_e}}\exp\left(-\frac{U_{float} + U_{bias}}{T_e}\right). \tag{B.1}$$

from which the electron density can then be calculated. This method needs an estimate for the electron temperature. This can be found from the exponential part of the bias sweep just below U_{float} (Morooka et al., 2011).

B.2. Ion density

The current on the negative bias voltage is given by (Wahlund et al., 2005)

$$I = I_{i,o}\left(1 - \frac{U_{bias}}{T_{i,eff}}\right) + I_{ph} \tag{B.2}$$

where

$$T_{i,eff} = T_i + \frac{m_i v_i^2}{2e} \tag{B.3}$$

is the effective ion energy and is given by the sum of a random ion temperature, directed flow energy, and I_{ph}, the photoelectron current. The following assumptions have been made. (1) The current is dominated by nano-grains and negative ions are disregarded. This then results in a straight line fit to the current. (2) The energy of the positive ions is dominated by the ram flux and not the thermal energy. (3) The photoelectron current is assumed to be constant. The total current on the negative side of the bias voltage is then given by (Wahlund et al., 2005; Morooka

et al., 2011; Holmberg et al., 2012; Shebanits et al., 2013)

$$I_{\text{tot}} \approx -\frac{1}{4} e A_{\text{LP}} | v_i | n_i \left(1 - \frac{2e U_{\text{bias}}}{m_i v_i^2} \right) + I_{\text{ph}} \tag{B.4}$$

The fit to the curve is linear and can be written as

$$I = m + b U_{\text{bias}} + I_{\text{ph}} \tag{B.5}$$

where the 'DC' level and the slope are given by

$$m = -\frac{1}{4} e A_{\text{LP}} | v_i | n_i + I_{\text{ph}} \propto n_i v_i \tag{B.6}$$

$$b = e A_{\text{LP}} | v_i | n_i \frac{e}{2 m_i v_i^2} \propto \frac{n_i}{v_i}, \tag{B.7}$$

respectively. Thus the ion density is estimated by multiplying m with b

$$m \cdot b \propto n_i^2. \tag{B.8}$$

Appendix C. Error estimation

C.1. Langmuir probe: 20 Hz

The error depends on the sweep signal strength as well as the type of parameter to be estimated. Holmberg et al. (2014) have estimated an error for the ion density of less than 30% in the plasma disk close to Enceladus. The error in the electron density, as well as in the floating potential estimates, are less than 10% and the error in the electron temperature is estimated to be less than 20% in the plasma disk region (Gustafsson and Wahlund, 2010).

From Eq. (6) we have a proportionality of the electron current, I_e, with the following parameters:

$$I_e \propto \begin{cases} n_e \\ 1/\sqrt{T_e} \\ U_{\text{float}} \end{cases} \tag{C.1}$$

The electron number densities used in this study vary with 4 orders of magnitude. We find that the spacecraft potential in flyby E6 varies a maximum of $\Delta U_{\text{SC}} \approx 3$ V giving, for the minimum T_e of 1 eV, a maximum of factor of 3 variation to the electron density, bottom panel Fig. 15. The electron temperature varies between 1 and 3 eV, see the middle panel in Fig. 15. The contribution of the electron temperature variation can be up to 0.6 due the $1/\sqrt{T_e}$ dependence. This is a small contribution considering that the current can vary 4 orders of magnitudes. However when calibrating for these two effects, the spacecraft potential as well as the electron temperature can cause a discrepancy in electron density estimates between the Langmuir probe 20 Hz sampled current based on theoretical expressions and sweep values of T_e and U_{SC} and the upper hybrid frequency derived value. This is why we chose to calibrate the probe current to f_{uh}, where the maximum errors should be as discussed here, and the real errors mostly far below these upper limits.

C.2. Langmuir probe: sweep

Another source of error in the 20 Hz electron density estimate is found in the current voltage characteristics inside the plume. A sweep in the dense plume region is presented in Fig. 16. The linear part of the curve ends before the bias potential at $+11.5$ V. This means that the electron density is no longer directly proportional to the Langmuir probe current and is underestimated in the central plume region. The effect is due to that the sampled current saturates in this dense plume plasma. The error in this particular sweep is $\approx 50\%$, causing an underestimation by a factor of 2. The

error can reach 88%. Note this effect can only cause underestimations.

C.3. Upper hybrid frequency determination

Three error sources can be distinguished for the upper hybrid density estimation. The first one is in the frequency resolution of the upper hybrid emission line which is estimated to be about 10%. In Fig. 13 we see that the upper hybrid emission line varies about 2 kHz. This translates to an electron density variation of 4 cm^{-3}. Using this variation for a flyby with the lowest electron density in the plasma disk of 40 cm^{-3} gives an error of 10%. The errors due to the magnetic field are small in comparison and can be neglected.

In summary, these errors are relatively small compared to the 20 Hz LP estimates of the electron density, and the upper hybrid emissions can therefore be used as a calibration method for the plasma disk 20 Hz LP current.

References

Burton, M.E., Dougherty, M.K., Russell, C.T., 2010. Saturn's internal planetary magnetic field. Geophys. Res. Lett. 37 (December (24)).

Cravens, T.E., McNutt, R.L., Waite, J.H., Robertson, I.P., Luhmann, J.G., Kasprzak, W., Ip, W.-H., 2009. Plume ionosphere of Enceladus as seen by the Cassini ion and neutral mass spectrometer. Geophys. Res. Lett. 36 (April), 8106.

Dong, Y., Hill, T.W., Ye, S.-Y., 2015. Characteristics of ice grains in the Enceladus plume from Cassini observations. J. Geophys. Res.: Sp. Phys. 120 (February (2)), 915–937.

Dougherty, M.K., Kellock, S., Southwood, D.J., Balogh, A., Smith, E.J., Tsurutani, B.T., Gerlach, B., Gleim, F., Russell, C.T., Erdos, G., Neubauer, F.M., Cowley, S. W.H., 2004. The Cassini magnetic field investigation. Sp. Sci. Rev. (114), 331–383.

Dougherty, M.K.K., Khurana, K.K.K., Neubauer, F.M.M., Russell, C.T.T., Saur, J., Leisner, J.S.S., Burton, M.E.E., 2006. Identification of a dynamic atmosphere at Enceladus with the Cassini Magnetometer. Science 311 (March (5766)), 1406–1409.

Fahleson, U., Fälthammar, C.-G., Pedersen, A., 1974. Ionospheric temperature and density measurements by means of spherical double probes. Planet. Sp. Sci. 22 (January (1)), 41–66.

Farrell, W., Wahlund, J.-E., Morooka, M., Gurnett, D., Kurth, W., MacDowall, R., 2014. An estimate of the dust pickup current at Enceladus. Icarus 239 (September), 217–221.

Farrell, W.M., Kurth, W.S., Tokar, R.L., Wahlund, J.-E., Gurnett, D.A., Wang, Z., MacDowall, R.J., Morooka, M.W., Johnson, R.E., Waite, J.H., 2010. Modification of the plasma in the near-vicinity of Enceladus by the enveloping dust. Geophys. Res. Lett. 37 (October), 20202.

Farrell, W.M.W.M., Wahlund, J.-E.J.-E., Morooka, M., Gurnett, D.a.D.A., Kurth, W.S.W.S., MacDowall, R.J.R.J., 2012. The electromagnetic pickup of submicron-sized dust above Enceladus's northern hemisphere. Icarus 219 (May (1)), 498–501.

Fleshman, B.L.L., Delamere, P.A.a., Bagenal, F., 2010. Modeling the Enceladus plume-plasma interaction. Geophys. Res. Lett. 37 (February (3)).

Gurnett, D., Grün, E., Gallagher, D., Kurth, W., Scarf, F., 1983. Micron-sized particles detected near Saturn by the Voyager plasma wave instrument. Icarus 53 (2), 236–254.

Gurnett, D.A.a., Averkamp, T.F.F., Schippers, P., Persoon, A.M.M., Hospodarsky, G.B.B., Leisner, J.S.S., Kurth, W.S.S., Jones, G.H.H., Coates, A.J.J., Crary, F.J.J., Dougherty, M.K.K., 2011. Auroral hiss, electron beams and standing Alfvén wave currents near Saturn's moon Enceladus. Geophys. Res. Lett. 38 (June (6)).

Gurnett, D.A.A., Kurth, W.S.S., Kirchner, D.L.L., Hospodarsky, G.B.B., Averkamp, T.F.F., Zarka, P., Lecacheux, A., Manning, R., Roux, A., Canu, P., Galopeau, P., Meyer, A., Gustafsson, G., Wahlund, J.-E., Ahlen, L., Rucker, H.O.O., Kaiser, M.L.L., Desch, M.D.D., Farrell, W.M.M., Harvey, C.C.C., Louarn, P., Cornilleau-Wehrlin, N., Boström, R., Åhlen, L., Ladreiter, H.P., Macher, W., Woolliscroft, L.J.C., Alleyne, H., Kellogg, P.J., Goetz, K., Pedersen, A., 2004. The Cassini radio and plasma wave investigation. Sp. Sci. Rev. 114 (September (4)), 395–463.

Gustafsson, G., Wahlund, J.-E., 2010. Electron temperatures in Saturns plasma disc. Planet. Sp. Sci. 58 (June (7–8)), 1018–1025.

Hill, T.W.W., Thomsen, M.F.F., Tokar, R.L.L., Coates, A.J.J., Lewis, G.R.R., Young, D.T.T., Crary, F.J.J., Baragiola, R.A.a., Johnson, R.E.E., Dong, Y., Wilson, R.J.J., Jones, G.H.H., Wahlund, J.-E., Mitchell, D.G.G., Horányi, M., 2012. Charged nanograins in the Enceladus plume. J. Geophys. Res. 117 (May (A5)), A05209.

Hillier, J.K., Green, S.F., McBride, N., Schwanethal, J.P., Postberg, F., Srama, R., Kempf, S., Moragas-Klostermeyer, G., McDonnell, J.A.M., Grun, E., 2007. The composition of Saturn's E ring. Mon. Not. R. Astron. Soc. 377 (June (4)), 1588–1596.

Holmberg, M., Wahlund, J.-E., Morooka, M., Persoon, a.M., 2012. Ion densities and velocities in the inner plasma torus of Saturn. Planet. Sp. Sci. 73 (December (1)), 151–160.

Holmberg, M.K.G., Wahlund, J.-E., Morooka, M.W., 2014. Dayside/nightside asymmetry of ion densities and velocities in Saturn's inner magnetosphere. Geophys. Res. Lett. 41 (June (11)), 3717–3723.

Horányi, M., Hartquist, T.W.W., Havnes, O., Mendis, D.A.A., Morfill, G.E.E., 2004. Dusty plasma effects in Saturn's magnetosphere. Reviews 42 (December (4)), 1–20.

Jia, Y.-D., Russell, C.T., Khurana, K.K., Toth, G., Leisner, J.S., Gombosi, T.I., 2010. Interaction of Saturn's magnetosphere and its moons. I. Interaction between corotating plasma and standard obstacles. J. Geophys. Res. (Sp. Phys.) 115 (April), 4214.

Jones, G.H., Arridge, C.S., Coates, A.J., Lewis, G.R., Kanani, S., Wellbrock, A., Young, D.T., Crary, F.J., Tokar, R.L., Wilson, R.J., Hill, T.W., Johnson, R.E., Mitchell, D.G., Schmidt, J., Kempf, S., Beckmann, U., Russell, C.T., Jia, Y.D., Dougherty, M.K., Waite, J.H., Magee, B.A., 2009. Fine jet structure of electrically charged grains in Enceladus' plume. Geophys. Res. Lett. 36 (August), 16204.

Kellock, S., Austin, P., Balogh, A., Gerlach, B., Marquedant, R., Musmann, G., Smith, E., Southwood, D., Szalai, S., 1996. Cassini dual technique magnetometer instrument (MAG). In: Horn, L. (Ed.), Society of Photo-Optical Instrumentation Engineers (SPIE) Conference Series, Society of Photo-Optical Instrumentation Engineers (SPIE)Conference Series. International Society for Optics and Photonics, vol. 2803, October 1996, pp. 141–152.

Kempf, S., Beckmann, U., Moragas-Klostermeyer, G., Postberg, F., Srama, R., Economou, T., Schmidt, J., Spahn, F., Grün, E., 2008. The E ring in the vicinity of Enceladus. Icarus 193 (February (2)), 420–437.

Kempf, S., Beckmann, U., Srama, R., Horanyi, M., Auer, S., Grün, E., 2006. The electrostatic potential of E ring particles. Planet. Sp. Sci. 54 (August (9–10)), 999–1006.

Kriegel, H., Simon, S., Meier, P., Motschmann, U., Saur, J., Wennmacher, A., Strobel, D.F., Dougherty, M.K., 2014. Ion densities and magnetic signatures of dust pickup at Enceladus. J. Geophys. Res.: Sp. Phys. 119 (April (4)), 2740–2774.

Kriegel, H., Simon, S., Motschmann, U., Saur, J., Neubauer, F.M., Persoon, A.M., Dougherty, M.K., Gurnett, D.A., 2011. Influence of negatively charged plume grains on the structure of Enceladus' Alfvén wings: hybrid simulations versus Cassini Magnetometer data. J. Geophys. Res. (Sp. Phys.) 116 (October (A15)), 10223.

Kriegel, H., Simon, S., Müller, J., Motschmann, U., Saur, J., Glassmeier, K.-H., Dougherty, M.M.K., 2009. The plasma interaction of Enceladus: 3D hybrid simulations and comparison with Cassini MAG data. Planet. Sp. Sci. 57 (December (14–15)), 2113–2122.

Krupp, N., Roussos, E., Kollmann, P., Paranicas, C., Mitchell, D.G., Krimigis, S.M., Rymer, A., Jones, G.H., Arridge, C.S., Armstrong, T.P., Khurana, K.K., 2012. The Cassini Enceladus encounters 2005–2010 in the view of energetic electron measurements. Icarus 218 (March), 433–447.

Kurth, W., Averkamp, T., Gurnett, D., Wang, Z., 2006. Cassini RPWS observations of dust in Saturn's E Ring. Planet. Sp. Sci. 54 (August (9–10)), 988–998.

Leisner, J.S., Hospodarsky, G.B., Gurnett, D.A., 2013. Enceladus auroral hiss observations: implications for electron beam locations. J. Geophys. Res.: Sp. Phys. 118 (January (1)), 160–166.

Medicus, G., 1962. Spherical Langmuir probe in "drifting" and "accelerated" Maxwellian distribution. J. Appl. Phys. 33 (June (10)), 3094.

Meier, P., Kriegel, H., Motschmann, U., Schmidt, J., Spahn, F., Hill, T.W., Dong, Y., Jones, G.H., 2014. A model of the spatial and size distribution of Enceladus dust plume. Planet. Sp. Sci. 104 (December), 216–233.

Morooka, M.W., Wahlund, J.-E., Eriksson, A.I., Farrell, W.M., Gurnett, D.A., Kurth, W.S., Persoon, A.M., Shafiq, M., André, H., Holmberg, M.K.G., 2011. Dusty plasma in the vicinity of Enceladus. J. Geophys. Res. (Sp. Phys.) 116 (December (A15)), 12221.

Mott-Smith, H., Langmuir, I., 1926. The theory of collectors in gaseous discharges. Phys. Rev. 28 (October (4)), 727–763.

Ness, N.F., Acuna, M.H., Lepping, R.P., Burlaga, L.F., Behannon, K.W., Neubauer, F.M., 1979. Magnetic field studies at jupiter by voyager 1: preliminary results. Science (New York, N.Y.) 204 (June (4396)) 982–987.

Neubauer, F., 1980. Nonlinear standing Alfvén wave current system at Io: theory. J. Geophys. Res. 85 (A3), 1171.

Omidi, N., Russell, C.T., Tokar, R.L., Farrell, W.M., Kurth, W.S., Gurnett, D.A., Jia, Y.D., Leisner, J.S., le Roux, J., Zank, G.P., Coates, A.J., Florinski, V., 2010. Hybrid simulations of plasma–neutral–dust interactions at Enceladus. In: Proceedings of the 9th Annual International Astrophysics Conference on Pickup Ions Throughout the heliosphere and beyond, vol. 1302, December 2010, AIP Publishing, Center 1305 Walt Whitman Road Suite 300 Melville, NY 1147-4300, USA, pp. 237–242.

Omidi, N., Tokar, R.L., Averkamp, T., Gurnett, D.A., Kurth, W.S., Wang, Z., 2012. Flow stagnation at Enceladus: the effects of neutral gas and charged dust. J. Geophys. Res. (Sp. Phys.) 117 (June), 6230.

Pontius, D.H., Hill, T.W., 2006. Enceladus: a significant plasma source for Saturn's magnetosphere. J. Geophys. Res.: Sp. Phys., 111.

Porco, C.C.C., Helfenstein, P., Thomas, P.C.C., Ingersoll, A.P.P., Wisdom, J., West, R., Neukum, G., Denk, T., Wagner, R., Roatsch, T., Kieffer, S., Turtle, E., McEwen, A., Johnson, T.V.V., Rathbun, J., Veverka, J., Wilson, D., Perry, J., Spitale, J., Brahic, A., Burns, J.A.A., DelGenio, A.D., Dones, L., Murray, C.D.D., Squyres, S., Delgenio, A.D., 2006. Cassini observes the active south pole of Enceladus. Science 311 (March 5766), 1393–1401.

Pryor, W.R., Rymer, A.M., Mitchell, D.G., Hill, T.W., Young, D.T., Saur, J., Jones, G.H., Jacobsen, S., Cowley, S.W.H., Mauk, B.H., Coates, A.J., Gustin, J., Grodent, D., Gérard, J.-C., Lamy, L., Nichols, J.D., Krimigis, S.M., Esposito, L.W., Dougherty, M.K., Jouchoux, A.J., Stewart, A.I.F., McClintock, W.E., Holsclaw, G.M., Ajello, J.M., Colwell, J.E., Hendrix, A.R., Crary, F.J., Clarke, J.T., Zhou, X., 2011. The auroral footprint of Enceladus on Saturn. Nature 472 (April), 331–333.

Saur, J., Neubauer, F.M., Schilling, N., 2007. Hemisphere coupling in Enceladus' asymmetric plasma interaction. J. Geophys. Res. 112 (November (A11)), A11209.

Shafiq, M., Wahlund, J.-E., Morooka, M.W., Kurth, W.S., Farrell, W.M., 2011. Characteristics of the dust–plasma interaction near Enceladus' South Pole. Planet. Sp. Sci. 59 (January), 17–25.

Shebanits, O., Wahlund, J.-E., Mandt, K., Ågren, K., Edberg, N., Waite, J., 2013. Negative ion densities in the ionosphere of Titan-Cassini RPWS/LP results. Planet. Sp. Sci. 84, 153–162.

Simon, S., Saur, J., Kriegel, H., Neubauer, F.M., Motschmann, U., Dougherty, M.K., 2011. Influence of negatively charged plume grains and hemisphere coupling currents on the structure of Enceladus' Alfvén wings: analytical modeling of Cassini magnetometer observations. J. Geophys. Res. 116 (April (A4)), A04221.

Simon, S., Saur, J., Treeck, S.C.V., Kriegel, H., Dougherty, M.K., 2014. Discontinuities in the magnetic field near Enceladus. Geophys. Res. Lett., 1–8.

Spahn, F., Schmidt, J., Albers, N., Hörning, M., Makuch, M., Seiss, M., Kempf, S., Srama, R., Dikarev, V., Helfert, S., Moragas-Klostermeyer, G., Krivov, A.V., Sremcevic, M., Tuzzolino, A.J., Economou, T., Grün, E., 2006. Cassini dust measurements at Enceladus and implications for the origin of the E ring. Science (New York, N.Y.) 311 (March (5766)) 1416–1418.

Spitale, J.N., Porco, C.C., 2007. Association of the jets of Enceladus with the warmest regions on its south-polar fractures. Nature 449 (October), 695–697.

Tokar, R.L., Wilson, R.J., Johnson, R.E., Henderson, M.G., Thomsen, M.F., Cowee, M.M., Sittler, J.C., Young, D.T., Crary, F.J., McAndrews, H.J., Smith, H.T., 2008. Cassini detection of water-group pick-up ions in the Enceladus torus. Geophys. Res. Lett. 35, 5–9.

Tokar, R.L.L., Johnson, R.E.E., Hill, T.W.W., Pontius, D.H.H., Kurth, W.S.S., Crary, F.J.J., Young, D.T.T., Thomsen, M.F.F., Reisenfeld, D.B.B., Coates, A.J.J., Lewis, G.R.R., Sittler, E.C.C., Gurnett, D.A.a., 2006. The interaction of the atmosphere of Enceladus with Saturn's plasma. Science 311 (March (5766)), 1409–1412.

Wahlund, J.-E., André, M., Eriksson, a.A.I.E., Lundberg, M., Morooka, M.W.M., Shafiq, M., Averkamp, T.T.F., Gurnett, D.D.A., Hospodarsky, G.B.G., Kurth, W.W.S.W., Jacobsen, K.K.S., Pedersen, a., Farrell, W., Ratynskaia, S., Piskunov, N., 2009. Detection of dusty plasma near the E-ring of Saturn. Planet. Sp. Sci. 57 (December (14–15)), 1795–1806.

Wahlund, J.-E., Boström, R., Gustafsson, G., Gurnett, D.A., Kurth, W.S., Averkamp, T., Hospodarsky, G.B., Persoon, A.M., Canu, P., Pedersen, A., Desch, M.D., Eriksson, A.I., Gill, R., Morooka, M.W., André, M., 2005. The inner magnetosphere of Saturn: Cassini RPWS cold plasma results from the first encounter. Geophys. Res. Lett. 32 (September (20)), 20.

Waite, J.H., Combi, M.R., Ip, W.-H., Cravens, T.E., McNutt, R.L., Kasprzak, W., Yelle, R., Luhmann, J., Niemann, H., Gell, D., Magee, B., Fletcher, G., Lunine, J., Tseng, W.-L., 2006. Cassini ion and neutral mass spectrometer: Enceladus plume composition and structure. Science (New York, N.Y.) 311 (March (5766)), 1419–1422.

Wang, Z., Gurnett, D., Averkamp, T., Persoon, A., Kurth, W., 2006. Characteristics of dust particles detected near Saturn's ring plane with the Cassini Radio and Plasma Wave instrument. Planet. Sp. Sci. 54 (9), 957–966.

Yaroshenko, V., Ratynskaia, S., Olson, J., Brenning, N., Wahlund, J.-E., Morooka, M., Kurth, W., Gurnett, D., Morfill, G., 2009. Characteristics of charged dust inferred from the Cassini RPWS measurements in the vicinity of Enceladus. Planet. Sp. Sci. 57 (December (14–15)), 1807–1812.

Yaroshenko, V.V., Lühr, H., Miloch, W.J., 2014. Dust charging in the Enceladus torus. J. Geophys. Res.: Sp. Phys. 119 (January (1)), 221–236.

Ye, S.-Y., Gurnett, D.A., Kurth, W.S., Averkamp, T., Kempf, S., Hsu, H.-W., Srama, R., Grün, E., 2014. Properties of dust particles near Saturn inferred from voltage pulses induced by dust impacts on Cassini spacecraft. J. Geophys. Res.: Sp. Phys. 119, 6294–6312.